Delft University of Technology

Electrical Engineering

Master Thesis

Wideband Flat Lenses Based on Artificial Dielectric Layers

Caspar Manuel Coco Martin
Defense date: September 14, 2022
Supervisor: dr. Daniele Cavallo

Wideband Flat Lenses Based on Artificial Dielectric Layers

Acknowledgements

This thesis summarizes the work done for ten months, preceded by a two-month internship, both at the Terahertz Sensing Group at Delft University of Technology.

A special thanks to dr. Daniele Cavallo, for always making time for discussions about which direction to take, for the clear explanations, a lot of patience, and for the guidance throughout the last year.

Furthermore, I would like to thank Sander van Katwijk for his guidance during the internship and for always being willing to share his knowledge and help.

I want to thank everyone in the group for their *gezelligheid* during our countless lunches, coffees, and Friday-afternoon drinks. This community makes every commute to Delft worthwhile.

To my friends who have suffered countless times, every time I *had* to share something antenna-related with them, thank you.

Finally, I want to thank my family and Iris, who have always supported me.

Wideband Flat Lenses Based on Artificial Dielectric Layers

This thesis is submitted in partial fulfillment of the requirements of the degree of

Master of Science

in

Electrical Engineering

by

Caspar Manuel Coco Martin

Student number:	4541936
Defense date:	Sept. 14, 2022
Thesis committee:	Prof. dr. Andrea Neto
	Dr. Daniele Cavallo
	Dr. Marco Spirito

List of Figures

Contents

Chapter 1

Introduction

1.1 Lens Antennas

Dielectric lenses are widely used quasi-optical components in imaging and antenna systems. They have been used for decades in applications such as radioastronomy, radar and satellite communications. Lens antennas provide high gain radiation characteristics and can support beam scanning capability by lateral displacement of the feed in the focal plane of the lens. Moreover, multiple beams can be generated simultaneously with a lens antenna system by placing multiple feeds in the focal plane. Each feed is then associated with a beam direction to form a so-called imaging array.

One disadvantage of the use of lenses in the microwave frequency range is the large weight and volume associated with the dielectric material composing the lens. However, the recent shift to higher operational frequencies (millimeter wave and terahertz bands) for radar and communication applications has resulted in a significant reduction of the antenna size and, in turn, in a renewed interest in lens antennas.

More specifically, recent advances in millimeter-wave (mmWave) technology for high-speed wireless communication and high-resolution radars have increased the popularity of dielectric lenses for multi-beam high-gain antennas [1]. Wireless communications in the near future will heavily rely on the possibility to transmit and receive multiple data streams through directive beams connecting the base station with different users. High-gain antennas operating in the mmWave frequency range will focus the radiation in smaller angular regions with the aim of improving the energy and spectral efficiency while reducing interference levels. Lens antennas are suitable low-cost candidates for multi-beam base stations serving multiple distributed users simultaneously. Similarly in automotive radar applications, directive lens antennas can be used to increase the range and angular resolution of car radar sensors, especially for long-range scenarios, with a moderate angular field of view.

1.1.1 Flat Lenses

A lens is a device that modifies the shape of the wavefront of an electromagnetic wave. For instance, a focusing lens can be used to convert a spherical wavefront generated by a point source into a planar wavefront, as shown in Fig. 1.1. To do so, the lens has to provide a phase shift that is larger in the center and smaller towards the lens edges, to compensate for the

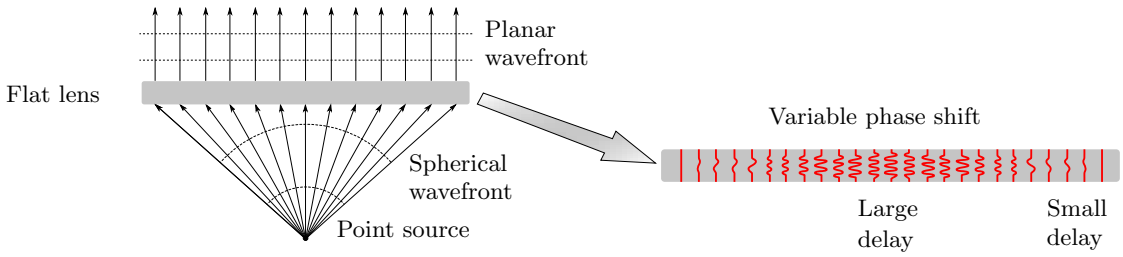

Figure 1.1: Focusing lens operating principle. A spherical wavefront is converted into a planar wavefront by a varying phase shift.

different path lengths of the rays emanating from the point source and impinging at different locations on the lens.

Flat lenses are a specific category of lenses, characterized by planar interfaces. The geometry in Fig. 1.1 refers to a flat lens. For such lenses, the phase shift is achieved by altering the material properties as a function of position. Typically, the refractive index of the material composing the lens is the highest in the center of the lens, where a large phase shift is required, and it gradually reduces towards the edges of the lens, where lower phase shifts are needed.

1.1.2 Phase Variation versus Lens Diameter and Focal Ratio

The key parameter for lens design is the maximum phase variation needed across the aperture, i.e. the phase difference between the center and the edge of the lens. For a lens characterized by focal length F and diameter D, the maximum phase variation depends the wavelength λ and the ratio of F to D, the F/D ratio. If the distance between the source and a point x on the lens is indicated as $L(x)$, the phase variation is given as $kL(x) - kF$, where $k = 2\pi/\lambda$ is the wavenumber.

For a given F/D ratio, the phase variation increases as the lens diameter D increases. In Fig. 1.2(a) the phase variation across a lens with $F/D = 0.5$ for different diameters is shown. A typical quadratic variation is observed for the phase profile across the lens. Similarly, for a given lens diameter, decreasing the focal length F also increases the phase variation. This is shown in Fig. 1.2(b) for a lens with $D = 10\lambda$.

1.1.3 Trade-off: Bandwidth vs Thickness

Conventional homogeneous dielectric lenses have excellent properties but are typically bulky and electrically thick. Flat lenses are low profile and can be fabricated more easily compared to curved lenses, making them desirable at mmWave frequencies. Planar multi-beam thin lens antennas can be realized as Fresnel lenses [2], transmitarrays [3], or metasurfaces [4]. Examples of such lenses are shown in Fig. 1.3(a) and Fig. 1.3(b).

Despite the very low profile, one of the limitations of these thin-lens solutions is the narrow frequency bandwidth due to the phase wrapping along the aperture, which results in sudden discontinuous jumps in the phase distribution. If the phase shift of the lens reaches a certain high value (ϕ), it can be reduced by an integer multiple of 360°, which corresponds to a local reduction of the lens thickness.

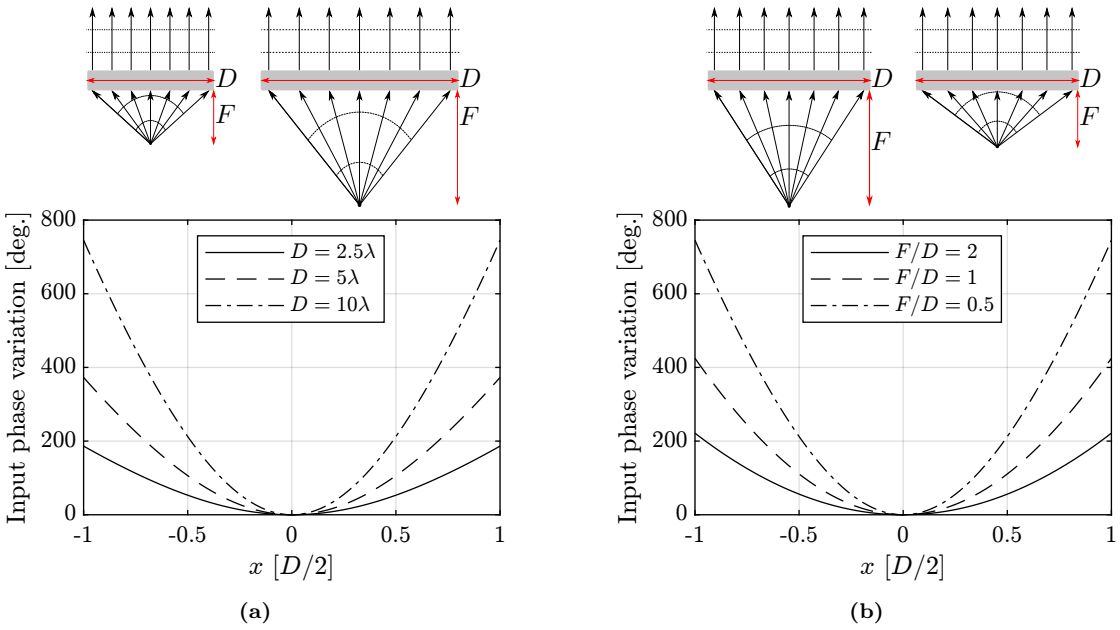

Figure 1.2: Phase variation for (a) different lens diameters D with $F/D = 0.5$ and (b) different F/D values, with diameter $D = 10\lambda$.

Fig. 1.4(a) shows an example of the phase shift through a lens that exceeds 360°. A lens providing this continuous phase variation is referred to as true-time-delay (TTD) and does not present bandwidth limitations. On the contrary, if the phase is wrapped in the range from 0 to 360°, as shown in Fig. 1.4(b), the bandwidth is limited. The point at which the phase discontinuity should occur is well defined only at a certain design frequency f_0, while it introduces phase errors at other frequencies.

Considering small deviations from f_0, and a maximum accepted phase error of 90°, for a lens with K zones, the bandwidth can be estimated as [5]

$$\mathrm{BW} \approx \frac{25}{K-1}\%\,. \tag{1.1}$$

For high gain lens antennas, a large diameter lens is required. This means there is a large phase variation which requires many zones K, which in turn limits bandwidth. As such, the bandwidth for lenses that use phase wrapping is inversely proportional to the directivity.

To overcome the bandwidth limitations, one can employ true-time-delay (TTD) lenses that provide wideband behavior, at the cost of increased thickness. One example of a TTD flat lens is the graded index (GRIN) lens, consisting of a dielectric cylinder with a radially changing refractive index [6]. In Fig. 1.3(c), a schematic side view of a GRIN lens is displayed. Since GRIN lenses have a varying refractive index, the reflection losses vary across the lens.

Hence, when designing flat lenses, a key trade-off to be considered is between bandwidth and thickness. However, one possibility to reduce the thickness of wideband TTD lenses is to use high-permittivity materials [7]. To reduce the reflection losses that would be caused by the high permittivity, matching layers must be employed to improve the transmission at the air-lens

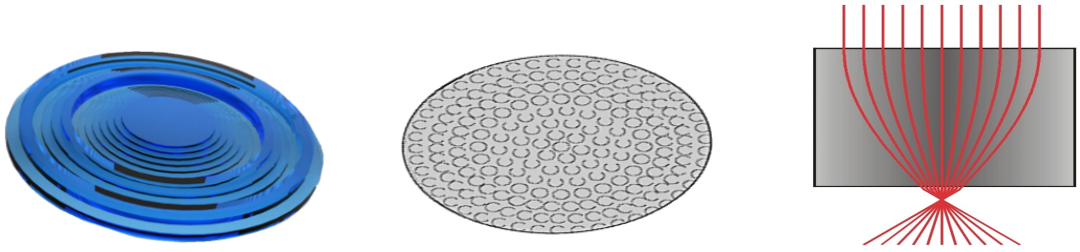

(a) (b) (c)

Figure 1.3: Different types of flat lenses: (a) Fresnel zone lens, (b) Metalens, (c) Graded index (GRIN) lens.

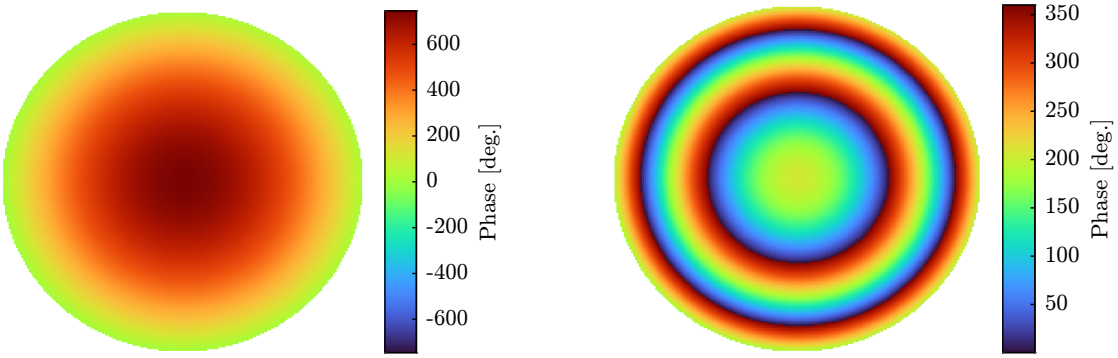

(a) (b)

Figure 1.4: Phase shift in degrees provided by flat lens as a function of position (a) without phase wrapping (true-time-delay) and (b) with phase wrapping.

interface [8]. In this work, artificial dielectric layers are investigated as the means to achieving high refractive indexes.

1.2 Artificial Dielectric Layers

A convenient way to realize high permittivity materials with refractive indexes that can be much larger than commercially available dielectrics is through the use of artificial dielectric layers [9]. Such artificial dielectrics can be realized as a cascade of periodic arrays composed of sub-wavelength patches, increasing the effective permittivity, thus providing an increased phase shift for waves propagating within the artificial medium. Very large effective permittivities can be achieved by stacking multiple of these layers. TTD lens designs based on periodic structures with sub-wavelength elements were presented in [10].

Recent advances in the analysis of artificial dielectric layers have resulted in closed-form expressions representing each layer's capacitance for general, non-periodic layer stacks [11]–[15]. These expressions include higher-order Floquet wave interaction between layers and thus they are accurate even for very small electrical inter-layer distances. The availability of analytical models allows estimating a unit cell's phase shift and scattering parameters with negligible computational resources.

A schematic cross-section of a lens based on artificial dielectric layers is depicted in Fig. 1.5. The patches are drawn as black lines and the density of the metal becomes larger in the center of the lens to implement the desired variation of effective refractive index.

Figure 1.5: Cross-section of a flat lens based on artificial dielectric layers. The black lines represent the metal patches in the dielectric host medium.

1.3 Objective of the Thesis

The goal of this thesis is to provide guidelines for the design of wideband flat lenses based on artificial dielectrics. Tradeoffs between achievable directivity and bandwidth are presented and linked to the technological constraints and manufacturing complexity. Moreover, a computationally efficient approach for the analysis of the lens is proposed based on a combination of the equivalent transmission line models of artificial dielectrics, geometrical optics (GO) / physical optics (PO) analysis of the feed primary pattern and the lens, and a ray tracing method through an equivalent anisotropic lens. Based on the tradeoff analysis and the modeling techniques, the design of a flat artificial dielectric lens with a certain desired bandwidth, directivity, and F/D can be efficiently performed. Example designs with various properties are also presented.

1.4 Outline

In Chapter 2 the theory of impedance transformers is used to define matching layers based on artificial dielectric layers (ADLs). The procedure to retrieve the effective refractive index for a given ADL stratification is reported, as well as the synthesis of the multi-section transformers in ADL technology. Moreover, closed-form expressions of the refractive index as a function of the angle of propagation inside the material are derived for both transverse magnetic (TM) and transverse electric (TE) plane waves.

Chapter 3 reports a tradeoff analysis between lens performance and manufacturing complexity. The study links the maximum phase variation required for a given lens design to the design parameters of the artificial dielectric, taking into account technology constraints, the total number of metal and dielectric layers, and overall thickness. A methodology for designing flat lenses based on ADLs is also presented. This starts with a design based on homogeneous dielectrics to realize the required phase shifts and low reflection and then replacing the homogeneous dielectrics with ADLs using the synthesis procedure described in Chapter 2. An example of a lens design is reported with F/D equal to 1.

In Chapter 4, the modeling method for the analysis of a flat lens based in ADLs is presented. This consists of a combined geometrical optics (GO) / physical optics (PO) approach, where each GO ray is studied as a plane wave problem to evaluate the reflection/transmission through each unit cell of the lens. Comparisons with full-wave simulations performed with CST are shown to validate the analysis method.

Chapter 5 presents a more complex procedure, taking into account the bending of rays within the lens. In fact, the GO/PO analysis in Chapter 4 assumes local periodicity of the unit cell for an

incident plane wave. This approximation becomes less accurate for large incidence angles, which occur in the periphery of the lens for small F/D or for a large off-focus displacement of the feed. For this reason, a ray tracing code for materials with a non-homogeneous isotropic refractive index was implemented and then generalized to anisotropic ADL-based effective materials. With this tool, improved accuracy can be achieved for the analysis of the lens, by accounting for the propagation of plane waves through multiple unit cells. Also, the directivity of the lens can be improved when accounting for this effect, especially for small F/D.

Lastly, Chapter 6 concludes with a review of the most significant results presented in this thesis and an outlook on possible future developments.

Chapter 2

Multisection Impedance Transformers from Artificial Dielectric Layers

When an electromagnetic wave impinges on an interface between two dielectrics with different refractive indexes, such as the interface of a flat lens, reflections usually occur. Matching layers can be used to reduce this reflection and to design a lens with low reflection losses over a large bandwidth. An arbitrary stratification of dielectric slabs, under plane-wave incidence, can be modeled using an equivalent transmission line model. In such a model, each layer of dielectric is represented by a transmission line section. The equivalent transmission line model can be used to translate impedance transformers from transmission line theory into a stack of dielectrics.

2.1 Impedance Transformers

Consider an infinite-length transmission line with characteristic impedance Z_0 connected to a load Z_L. For a voltage wave incident on the load, the voltage reflection coefficient Γ is defined as

$$\Gamma = \frac{Z_0 - Z_L}{Z_0 + Z_L}. \tag{2.1}$$

The reflection coefficient is 0 only if $Z_0 = Z_L$. For any other case, reflection occurs. For real load impedances, the simplest impedance transformer is the single-section quarter-wave transformer, shown in Fig. 2.1(a). A quarter wavelength transmission line section with characteristic impedance $Z_1 = \sqrt{Z_0 Z_L}$ is added between the infinite transmission line and the load. It ensures a perfect matching between the load and the transmission line at the design frequency. The bandwidth is inversely proportional to the transformation ratio $\max(Z_L, Z_0)/\min(Z_L, Z_0)$. In general, more transformer sections can be used to achieve matching over a wider bandwidth for a given transformation ratio.

2.1.1 Theory of Small Reflections

In a cascade of transmission lines, multiple reflections occur, making it difficult to express the overall reflection coefficient at a junction of two transmission lines. In [16] the *theory of small*

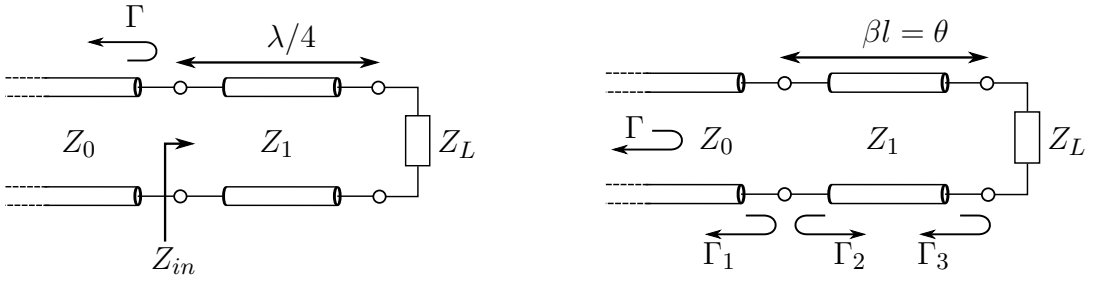

(a) **(b)**

Figure 2.1: (a) Transmission line circuit of quarter wave transformer. (b) Transmission line with reflection coefficients used to derive the theory of small reflections.

reflections is introduced, which will be briefly summarized below.

The analysis considers a transmission line section of length $\theta = \beta l$, connected to a load on one end, and to an infinite-length transmission line on the other end, as shown in Fig. 2.1(b). To find the overall reflection coefficient Γ for a wave arriving from the infinite transmission line, one considers all the (partial) reflections at Γ_1, Γ_2, and Γ_3. This results in a geometric series which can be expressed as

$$\Gamma = \frac{\Gamma_1 + \Gamma_3 e^{-2j\theta}}{1 + \Gamma_1\Gamma_3 e^{-2j\theta}}. \tag{2.2}$$

If Γ_1 and Γ_3 are small compared to 1, the overall reflection coefficient can be approximated as

$$\Gamma \approx \Gamma_1 + \Gamma_3 e^{-2j\theta}, \tag{2.3}$$

offering a first-order approximation of the overall reflection coefficient.

This first-order approximation can also be applied to an arbitrary number of transformer sections. A first-order approximation of the overall reflection coefficient Γ for an N-section transformer can be written as

$$\Gamma(\theta) = \Gamma_0 + \Gamma_1 e^{-2j\theta} + \Gamma_2 e^{-4j\theta} + \cdots + \Gamma_N e^{-2jN\theta}. \tag{2.4}$$

If one imposes the reflection coefficients to be symmetric, i.e. $\Gamma_0 = \Gamma_N$, $\Gamma_1 = \Gamma_{N-1}$ etc., this yields

$$\Gamma(\theta) = e^{-jN\theta}\left[\Gamma_0(e^{jN\theta} + e^{-jN\theta}) + \Gamma_1(e^{j(N-2)\theta} + e^{-j(N-2)\theta}) + \cdots\right], \tag{2.5}$$

which can be written as a cosine series

$$\Gamma(\theta) = \begin{cases} 2e^{-jN\theta} \displaystyle\sum_{n=0}^{(N-1)/2} \Gamma_n \cos((N-2n)\theta) & N \text{ odd} \\ 2e^{-jN\theta} \left(\displaystyle\sum_{n=0}^{N/2-1} \Gamma_n \cos((N-2n)\theta) + \frac{1}{2}\Gamma_{N/2} \right) & N \text{ even} \end{cases} \tag{2.6}$$

From this expression, it follows that by adequately choosing the reflection coefficients at each junction Γ_n, a variety of matching responses can be designed. Several examples of such transformers are shown in Fig. 2.2(a). Generally, the bandwidth increases as more transformer sections are added.

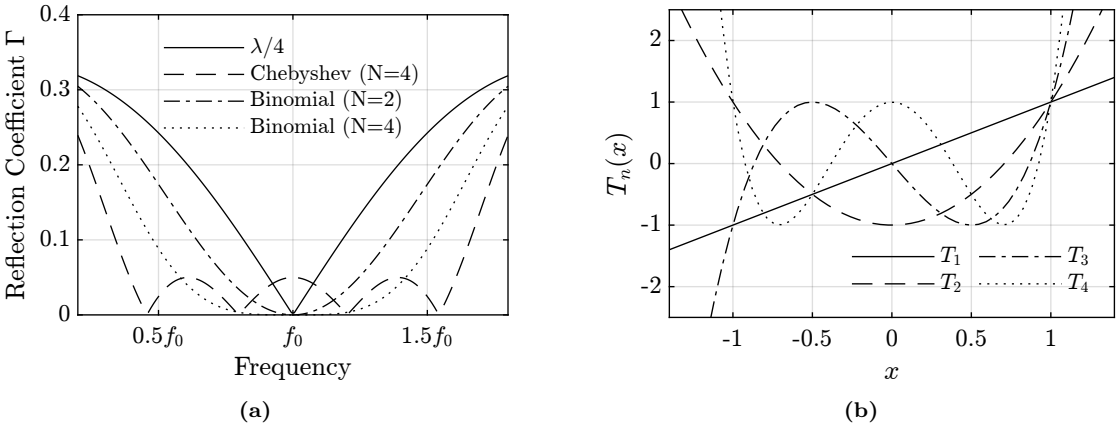

Figure 2.2: (a) Frequency responses of different impedance transformers, to match a transformation ration of $Z_L/Z_0 = 2$. (b) Chebyshev polynomials $T_n(x)$ for $n = 1, 2, 3, 4$.

In [17], the derivations of several multi-section impedance transformers are given, such as exponentially tapered transformers, the binomial transformer, and the Chebyshev transformer. The derivation for the Chebyshev transformer, however, is only given for up to $N = 4$ sections. In the next section, a closed form expression for the reflection coefficients of the Chebyshev transformer of arbitrary order N is derived.

2.1.2 Chebyshev Transformer of Arbitrary Order N

The Chebyshev transformer is based on the Chebyshev polynomials, and maximizes the bandwidth of the transformer, at the cost of a ripple in the passband. The nth-order Chebyshev polynomial is a polynomial of degree n, denoted by $T_n(x)$. The first two Chebyshev polynomials are

$$T_0(x) = 1 \tag{2.7}$$

$$T_1(x) = x \tag{2.8}$$

For all higher order Chebyshev polynomials, one can apply iteratively

$$T_n(x) = 2xT_{n-1}(x) - T_{n-2}(x). \tag{2.9}$$

In Fig. 2.2(b), the first four Chebyshev polynomials are plotted. The Chebyshev polynomials have some useful properties. For $x \in [-1, 1]$, the polynomials oscillate between -1 and 1, which is used to create an equal-ripple passband. To do so, $x = -1$ and $x = 1$ are mapped to the start and end of the passband respectively by substituting $x = \cos\theta \sec\theta_m$, where $\sec\theta_m$ is a parameter depending on the transformation ratio Z_L/Z_0 and the pass band ripple Γ_m and can be approximated as

$$\sec\theta_m \approx \cosh\left[\frac{1}{N}\cosh^{-1}\left(\left|\frac{\ln(Z_L/Z_0)}{2\Gamma_m}\right|\right)\right]. \tag{2.10}$$

To synthesize an N-section Chebyshev transformer, with an equal-ripple passband, the overall reflection coefficient is made proportional to the Chebyshev polynomial:

$$\Gamma(\theta) = Ae^{-jN\theta}T_N(\sec\theta_m \cos\theta). \tag{2.11}$$

The constant A can be found by imposing the boundary condition (letting $\theta = 0$, corresponding to zero frequency) as

$$A = \frac{Z_L - Z_0}{Z_L + Z_0} \frac{\Gamma_m}{\left| \frac{Z_L - Z_0}{Z_L + Z_0} \right|}. \tag{2.12}$$

To find the values of the impedances Z_n in the multi-section transformer one can equate Eq. (2.6) to Eq. (2.11):

$$N \text{ odd} \qquad 2e^{-jN\theta} \sum_{n=0}^{(N-1)/2} \Gamma_n \cos((N-2n)\theta) = Ae^{-jN\theta} T_N(\sec\theta_m \cos\theta) \tag{2.13}$$

$$N \text{ even} \qquad 2e^{-jN\theta} \left(\sum_{n=0}^{N/2-1} \Gamma_n \cos((N-2n)\theta) + \frac{1}{2}\Gamma_{N/2} \right) = Ae^{-jN\theta} T_N(\sec\theta_m \cos\theta) \tag{2.14}$$

It can be shown (full derivation in Appendix A) that for an arbitrary number of sections N, each Γ_n can be expressed in closed form as

$$\Gamma_n = \begin{cases} A\frac{N}{4} \sum_{n'=0}^{\lfloor \frac{N}{2} \rfloor} \sum_{p=0}^{N-2n'} a(n', p, N)(\sec\theta_m)^{N-2n'} U(n' + p \in [n, N-n]) & N \text{ odd} \\ A\frac{N}{4} \sum_{n'=0}^{\lfloor \frac{N}{2} \rfloor} \sum_{p=0}^{N-2n'} a(n', p, N)(\sec\theta_m)^{N-2n'} U(n' + p \in [n, N-n]) & N \text{ even, } n < N/2 \\ A\frac{N}{2} \sum_{n'=0}^{\lfloor \frac{N}{2} \rfloor} \sum_{p=0}^{N-2n'} a(n', p, N)(\sec\theta_m)^{N-2n'} U(n' + p \in [n, N-n]) & N \text{ even, } n = N/2 \end{cases} \tag{2.15}$$

where

$$U(n' + p \in [n, N-n]) = \begin{cases} 1 & \text{for } n' + p = n \text{ or } n' + p = N - n \\ 0 & \text{otherwise} \end{cases} \tag{2.16}$$

and

$$a(n', p, N) = (-1)^{n'} \frac{(N - n' - 1)!}{n'!p!(N - 2n' - p)!} \tag{2.17}$$

Note that for N even, $n > N/2$, Γ_n can be found by applying symmetry, since we imposed this condition.

Finally, from Γ_n, the impedance of the sections can be found as

$$Z_{n+1} \approx e^{(\ln(Z_n) + 2\Gamma_n)} \tag{2.18}$$

referring to Fig. A.1 in Appendix A.

2.2 Artificial Dielectric Layers Analysis

To create materials with specific properties, which can for example be used to realize impedance transformers or high permittivity materials, artificial dielectric layers can be used.

Artificial dielectrics are materials in which the dielectric permittivity does not arise from the polarization effect at the atomic or molecular level, but is artificially constructed by including

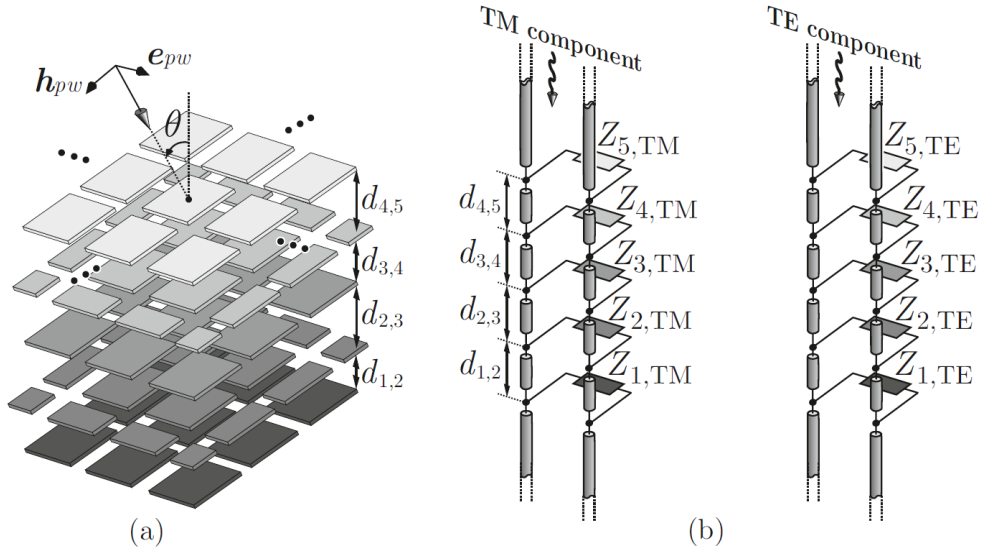

Figure 2.3: (a) Schematic of ADL and (b) the corresponding equivalent transmission lines for TE- and TM-mode. Source: [15]

metal structures. The artificial dielectric used in this work uses a periodic arrangement of small flat metal patches, visualized in Fig. 2.3a. These artificial dielectric layers (ADLs) can be analyzed using closed-form expressions which were first presented in [11], [12]. The analysis was later extended to include shifts between the layers in [13], and then further generalized to allow stacks of non-identical patches in [15].

The analysis is valid for an infinitely repeating unit cell in the x- and y-direction. A schematic drawing of an ADL is given in Fig. 2.3(a). This unit cell consists of a stack of metal and dielectric layers, and is repeated with period p. Each metal layer has a certain gap width w, shift s relative to the adjacent metal layers, and distance d to the adjacent metal layers. In Fig. 2.4, the geometry of the unit cell is detailed. Each dielectric layer has a certain thickness h and permittivity ε_r.

The dielectric layers between the metal layers are modeled as transmission line sections. The metal layers are modeled as shunt impedances, where the impedance of each metal layer is given by:

$$Z_{n,TM} = \frac{-j}{B_n} \tag{2.19}$$

$$Z_{n,TE} = \frac{-j}{B_n \left(1 - \frac{k_\rho^2}{2k_{\text{layer}}^2}\right)} \tag{2.20}$$

Where $k_\rho^2 = k_x^2 + k_y^2$ and k_{layer} is the wavenumber of the dielectric around the metal layer, which can be approximated as the average wavenumber of the dielectric above and below. In Equation

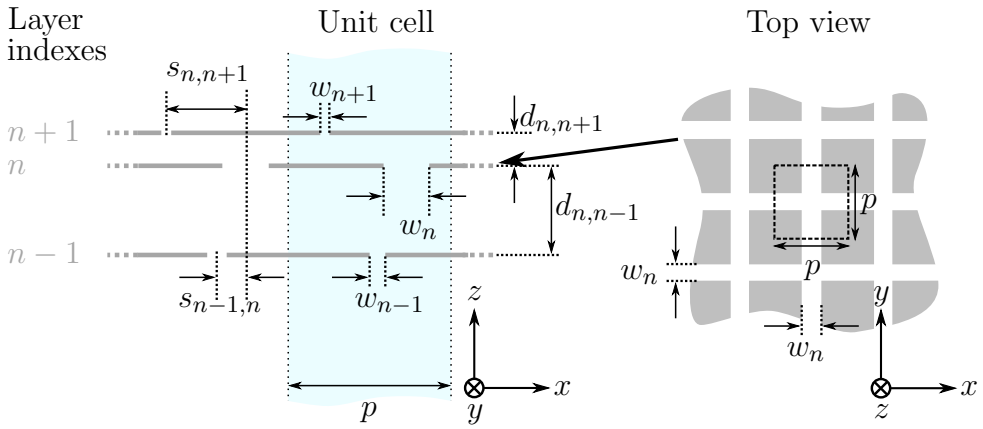

Figure 2.4: Geometry of layer n of the ADL, and the adjacent layers above and below.

2.19 and 2.20, the susceptance B_n is defined as [15]:

$$B_n = jp\varepsilon f \sum_{m\neq 0} \{S_m(w_n)\left[f_m(d_{n,n+1}) + f_m(d_{n-1,n})\right] + S_m(w_{n+1})\, g_m(s_{n,n+1}, d_{n,n+1}) + S_m(w_{n-1})\, g_m(s_{n-1,n}, d_{n-1,n})\} \tag{2.21}$$

where ε is the permittivity around the layer, found from k_{layer}. f is the frequency under consideration, and m are the considered indexes of the Floquet modes. For the top and bottom layers, the limit is taken for $d_{n\pm1} \to \infty$. The functions $S_m(w)$, $f_m(d)$ and $g_m(s,d)$ are given by:

$$S_m(w) = \frac{\left|\operatorname{sinc}\left(\frac{\pi m w}{p}\right)\right|^2}{|m|} \tag{2.22}$$

$$f_m(d) = -\cot\left(\frac{-2j\pi|m|d}{p}\right) \tag{2.23}$$

$$g_m(s,d) = e^{j2\pi m s/p} \csc\left(\frac{-2j\pi|m|d}{p}\right). \tag{2.24}$$

The equivalent transmission lines for this structure under an incident TE- or TM-polarized plane wave are shown in Fig. 2.3(b). The characteristic impedance of the transmission line sections for the transverse electric (TE)- and transverse magnetic (TM)-mode are given by

$$Z_{0,TE} = \frac{k_0\sqrt{\varepsilon_{r,d}}}{k_{z,d}} \tag{2.25}$$

$$Z_{0,TM} = \frac{k_{z,d}}{k_0\sqrt{\varepsilon_{r,d}}}. \tag{2.26}$$

At frequency f, the free-space wave number can be expressed as

$$k_0 = \frac{2\pi f}{c_0} \tag{2.27}$$

where c_0 is the speed of light in the vacuum. Given a certain angle of incidence in the medium with permittivity $\varepsilon_{r,s}$ surrounding the stratification, one can find k_ρ as

$$k_\rho = \sqrt{\varepsilon_{r,s}} k_0 \sin\theta \,. \tag{2.28}$$

Since k_ρ remains constant as the wave propagates through different dielectric slabs with horizontal interfaces as a consequence of Snell's law, k_z must change in different media, to satisfy the condition $k = \sqrt{k_z^2 + k_\rho^2}$. Using this, $k_{z,d}$ in a dielectric layer with refractive index $\sqrt{\varepsilon_{r,d}}$ can be expressed as a function of the angle outside the stratification as

$$k_{z,d} = -j\sqrt{-(k_0^2 \varepsilon_{r,d} - k_\rho^2)} = k_0 \sqrt{\varepsilon_{r,d}} \, |cos\theta| \,, \tag{2.29}$$

which is the propagation constant of the equivalent transmission line section. The length of the transmission line is defined by the vertical spacing of the metal layers d.

2.2.1 Evaluation of ADL in Arbitrary Stratification

With an expression for the capacitance of each metal layer, the scattering parameters for an arbitrary stack-up can be evaluated. This is done by finding the ABCD matrix of each element of the transmission line and computing the matrix product of all ABCD matrices.

Dielectric Slab

The ABCD matrix of a lossless transmission line section, which represents a dielectric layer, is given by

$$\begin{bmatrix} \cos(k_{z,d}d) & jZ_{0,Ti}\sin(k_{z,d}d) \\ \frac{1}{Z_{0,Ti}} j\sin(k_{z,d}d) & \cos(k_{z,d}d) \end{bmatrix} \tag{2.30}$$

where $Z_{0,Ti}$ refers to the transmission line's characteristic impedance for either TE- or TM-mode.

The ABCD matrix of a shunt impedance Z is given by

$$\begin{bmatrix} 1 & 0 \\ \frac{1}{Z_{n,Ti}} & 1 \end{bmatrix}. \tag{2.31}$$

Total ABCD matrix

With each ABCD matrix known, the total ABCD matrix is computed as the matrix product of the individual ABCD matrices:

$$ABCD_{\text{total},Ti} = \prod_{i=1}^{N} ABCD_{i,Ti} \tag{2.32}$$

From the ABCD matrix, one can find the S-parameters for arbitrary source and load impedances Z_S and Z_L with the equations described in [18].

The S_{11} of a two-port between a source impedance Z_S and load impedance Z_L is given by

$$S_{11} = \frac{AZ_L + B - CZ_S^* Z_L - DZ_S^*}{AZ_L + B + CZ_S Z_L + DZ_S}. \tag{2.33}$$

The S_{12} of such a two-port is given by

$$S_{12} = \frac{2(AD - BC)\sqrt{\Re(Z_S)\Re(Z_L)}}{AZ_L + B + CZ_S Z_L + DZ_S} \tag{2.34}$$

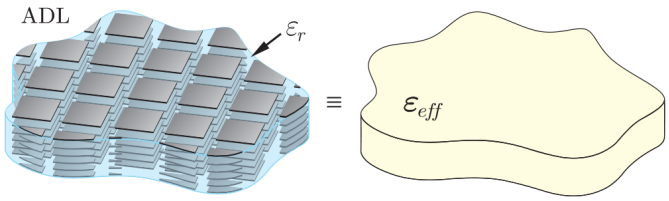

Figure 2.5: Artificial dielectric layers (ADL) in host medium ε_r (left) and the homogenized version (right). Source: [19]

2.3 Effective Refractive Index

The artificial dielectric layers form a material that behaves as if the permittivity and permeability are different from the host dielectric. Homogenization techniques can be used to find this effective permittivity and permittivity, and the refractive index. In Fig. 2.5, the main idea of homogenization is visualized: a complex structure is simplified to a dielectric with an effective refractive index, such that the response to electromagnetic waves is similar to the original structure. Different methods can be used to find the effective refractive index given a certain ADL geometry. The method described in [20] uses S-parameters from normal and oblique incidence to find, with knowledge of the thickness of the structure, the complete effective tensors for both the permittivity and permeability. If one is interested only in finding the refractive index for a certain angle, one can equate the ABCD matrix of a stratification to the ABCD matrix of a homogeneous transmission line. This method is described in [21] and will be outlined here.

2.3.1 Extraction of Effective Refractive Index

The method works by equating the ABCD matrix of a shunt impedance connected between two equal-length transmission line sections, to the ABCD matrix of a single transmission line section. Note that a similar analysis could be applied to an arbitrary stratification.

Computing the matrix product of two transmission line sections of length $d/2$, with the shunt impedance Z_{ADL} in between, and equating A of the resulting ABCD matrix with A from Eq. (2.30), one can write

$$k_{z,\text{eff},Ti} = \frac{1}{d}\cos^{-1}\left(\cos(k_z d) + j\frac{Z_{Ti}}{2Z_{ADL,Ti}}\sin(k_z d)\right), \tag{2.35}$$

where the metal layer impedance $Z_{ADL,Ti}$, is given by

$$Z_{ADL,TE} = -\frac{j}{B_s\left(1 - \frac{\sin^2\theta}{2}\right)} \tag{2.36}$$

$$Z_{ADL,TM} = -\frac{j}{B_s} \tag{2.37}$$

Now, one can find the effective refractive index as

$$n_{Ti}^2 = \frac{k_{z,\text{eff},Ti}^2 + k_\rho^2}{k_0^2}. \tag{2.38}$$

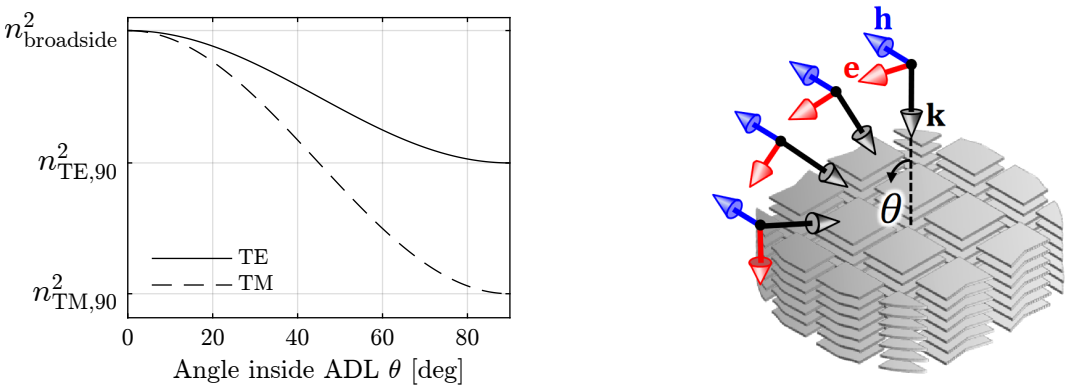

(a) (b)

Figure 2.6: (a) Effective refractive index in ADL as a function of angle θ inside the material, for TE- and TM-mode. (b) TM-mode plane wave incident on ADL with angle θ.

2.3.2 Closed Form Expression for Angle Dependence of Refractive Index

While the method above allows extracting the effective refractive index given a specific ADL geometry, having a general relationship between the broadside refractive index in an ADL and the refractive index at an angle, without specifying the geometry of the ADL would be helpful. This information is for example useful for a simple generalization of ray tracing methods in inhomogeneous media to account for the anisotropy, as will be shown in Chapter 5.

The effective refractive index in an ADL as a function of angle θ inside the ADL is plotted in Fig. 2.6(a). The variation between $n^2(\theta = 0°)$ and $n^2_{Ti}(\theta = 90°)$ can be approximated with a $\cos^2\theta$ shape for practical ADL designs, as follows:

$$n^2_{Ti}(\theta) \approx (n^2(\theta = 0°) - n^2_{Ti}(\theta = 90°))\cos^2\theta + n^2_{Ti}(\theta = 90°). \tag{2.39}$$

Therefore, to fully characterize the ADL in terms of its effective refractive index, given the broadside ($\theta = 0°$) effective refractive index, only the refractive index for $\theta = 90°$ for both TE- and TM-mode is required.

TM-Mode

For the TM-mode, the behavior for a broadside wave is identical to the TE-mode, because in both cases the field is parallel to the metal patches. For a wave incident at $\theta = 90°$, the E-field in the TM-wave is perpendicular to the metal patches, as can be seen in Fig. 2.6(b). There is no interaction with the patches in this case, and the effective refractive index is equal to the refractive index of the host material.

This can also be observed from the equations. For TM mode, Z_{Ti} in Eq. (2.35) is given by $Z_{Ti} = Z_{TM} = \zeta k_z/k$. It follows that if $\theta = 90°$, k_z is 0, and thus $k_{z,\text{eff},TM} = 0$. Then, the refractive index is given by

$$n^2_{TM}(\theta = 90°) = \frac{k_\rho^2}{k_0^2} = n^2_{\text{host}}. \tag{2.40}$$

TE-mode

For TE-mode, the broadside case is equivalent to TM mode. However, when $\theta = 90°$ the E-field is still parallel with the plane where the metal patches lie, although the direction of propagation has changed. To arrive at an expression for the effective refractive index for $\theta = 90°$, given a broadside effective refractive index $n(\theta = 0°)$, the first step is to write B_s in terms of $n(\theta = 0°)$. Substitute Eq. (2.36) in Eq. (2.35) and use $Z_{TE} = \zeta k/k_z$, yields

$$\cos(k_{z,\text{eff},TE}d) = \cos(k_z d) + \frac{j}{2}\frac{\zeta k}{k_z}\left(-\frac{j}{B_s\left(1-\frac{\sin^2\theta}{2}\right)}\right)^{-1}\sin(k_z d). \tag{2.41}$$

If $\theta = 0°$, $k_z = k$, and one can write

$$k_{z,\text{eff},TE}(\theta = 0°) = \frac{1}{d}\cos^{-1}\left(\cos(kd) - \frac{\zeta B_s}{2}\sin(kd)\right) \tag{2.42}$$

Then, using $k_\rho = 0$ in Eq. (2.38), the refractive index can be related to $k_{z,\text{eff},TE}$ as

$$n_{TE}(\theta = 0°) = \frac{1}{k_0 d}\cos^{-1}\left(\cos(kd) - \frac{\zeta B_s}{2}\sin(kd)\right). \tag{2.43}$$

Solving for B_s yields

$$B_s = \frac{2}{\zeta}\frac{\cos(kd) - \cos(k_0 d n_{TE}(\theta = 0))}{\sin(kd)} \tag{2.44}$$

Now take $\theta = 90°$, from which follows that $k_z = 0$. Consider

$$\lim_{k_z \to 0}\frac{\sin(k_z d)}{k_z d} = 1. \tag{2.45}$$

Using this, Eq. (2.41) can be rewritten to

$$\cos(k_{z,\text{eff},TE}d) = 1 - \frac{\zeta k d B_s}{4} \tag{2.46}$$

Isolating $k_{z,\text{eff},TE}$, and applying Eq. (2.38), the effective refractive index for $\theta = 90°$ can be written as

$$n^2_{TE}(\theta = 90°) = n^2_{\text{host}} + \left(\frac{1}{k_0 d}\cos^{-1}\left(1 - \frac{\zeta k d B_s}{4}\right)\right)^2. \tag{2.47}$$

where B_s should be substituted with Eq. (2.44). Note that the only parameters of the ADL required in this equation are the vertical spacing between metal layers d and the refractive index of the host medium.

2.4 ADL Synthesis

Bringing together the transformer design, ADL analysis, and ADL homogenization, one can synthesize a unit cell in ADL technology with the scattering properties of an arbitrary transformer. The goal of this section is to describe how, given a transformer design, i.e. the number of sections N, the impedance Z_i of each section, and the length l_i of each section, a unit cell with the same

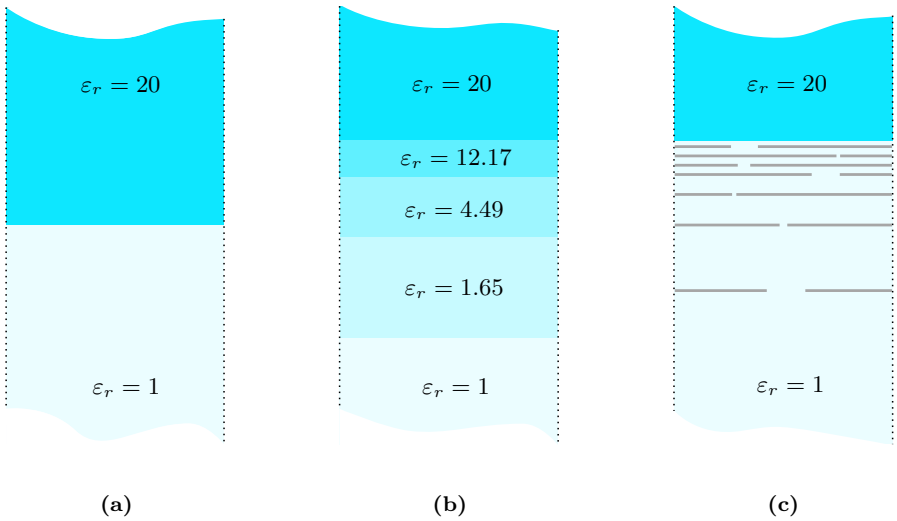

Figure 2.7: (a) Interface between two dielectrics. (b) Interface between two dielectrics with 3-section Chebyshev matching transformer. (c) Interface between two dielectrics with 3-section Chebyshev matching transformer, implemented using ADLs.

scattering properties can be designed. For the quarter wave transformer, binomial transformer, and Chebyshev transformer, the section length should be $\lambda/4$ taking into account the effective permittivity of that section. Thus, each section has a length of $\lambda_0/(4\sqrt{\varepsilon_r})$.

The impedance of each section is related to an effective permittivity. The relation is given by

$$\varepsilon_r = \left(\frac{Z_0}{Z}\right)^2, \tag{2.48}$$

with $Z_0 = 120\pi$. Each section starts with an initial number of metal layers. The effective permittivity of the section is evaluated. If the effective permittivity is higher than required, the gap width w is increased, or the horizontal shift s between the layers is reduced. Conversely, if the effective permittivity is lower than required, either the gap width should be reduced, or the shift should be increased. Considering manufacturing constraints, there will be minimum and maximum gap widths. If with the initial number of metal layers, no feasible design can be found, the number of metal layers should be altered.

After each section is synthesized independently, the reflection coefficient as a function of frequency for the complete stack is evaluated, and compared to the frequency of the transformer one tries to synthesize.

To improve the design, one could formulate the design of the unit cell as an optimization problem minimizing a specific cost function, with the design of each independently synthesized section as a starting point. For example, the absolute difference between the desired and achieved response over a certain frequency range could be used as a cost function to find values for the gap widths and inter-layer shifts:

$$\text{Cost} = \sum_{n=0}^{N-1} \left|\Gamma_{\text{desired}}(f[n]) - \Gamma(f[n])\right|. \tag{2.49}$$

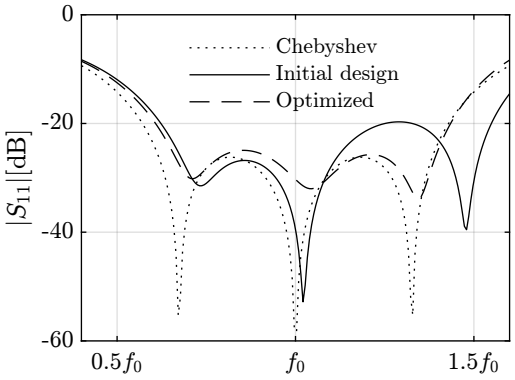

Figure 2.8: Reflection coefficient from an ideal 3-Chebyshev transformer, the same transformer implemented in ADL technology (Initial design), and the optimized version of this design (Optimized).

Alternatively, one could minimize the difference between the phase of the transmission coefficient and the required phase shift. Of course, there are limits to applying such an optimization technique, as the finite number of artificial dielectric layers does not always yield a perfect correspondence with the ideal transformer response. In general, increasing the number of metal layers, thus having more degrees of freedom in the design, reduces the difference with the desired response. This however comes at the cost of a more complex manufacturing process.

Example Transformer Design

Consider a 3-section Chebyshev transformer, to improve the matching at the interface between a dielectric slab with permittivity $\varepsilon_r = 20$ and a dielectric slab with permittivity $\varepsilon_r = 1$, as depicted in Fig. 2.7(a).

In a 3-section Chebyshev with a pass-band ripple of $\Gamma_m = 0.05$, the relative permittivities of the sections are 1.65, 4.49, and 12.17. Each section's length is $\lambda/4$. Implementing these matching layers as homogeneous dielectric layers results in the structure in Fig. 2.7(b).

From this stratification, ADL sections can be synthesized. Using a period of $p = 0.1\lambda_0$, and minimum gap width $w_{min} = 0.0017\lambda_0$, results in a design with 7 metal layers. In Fig. 2.8, the magnitude of the S_{11} of this stratification is plotted as a solid line. Depending on the requirements of the design, this could be acceptable. If a response more similar to the ideal response is desirable, the design can be improved using an optimization procedure. Applying an optimization with the cost function described in Eq. (2.49) to the initial design yields the optimized design. The response is more similar to the Chebyshev response. To further improve the design, one could do another design with more layers.

A cross-section drawing of the final design of the interface, with matching layers implemented as ADLs, is shown in Fig. 2.7(c).

Chapter 3

Tradeoff Analysis and Lens Unit Cell Design

3.1 Phase Variation

As explained in Chapter 1, a flat lens generates a collimated beam by converting a spherical wavefront into a planar wavefront. The lens has to provide a phase shift that is larger in the center and smaller towards the lens edges, to compensate for the different path lengths of the rays emanating from the point source and impinging at different locations on the lens. The key parameter for the design of TTD lenses is the maximum phase variation needed across the aperture, i.e. the phase difference between the center and the edge of the lens. The maximum phase variation depends on the lens diameter in terms of the wavelength and on the focal distance to lens diameter (F/D) ratio. In particular, for a given electrical size of the lens, the maximum phase variation increases for smaller F/D, because the smaller radius of curvature of the spherical wavefront causes larger differences in the path length of the impinging rays. Similarly, for a fixed F/D, the phase range increases as a function of the lens diameter. For designing a lens, one could generate a map of maximum phase variation for different values of lens diameter D and focal ratio F/D, as shown in Fig. 3.1(a). These values can then be related to the design parameters of the artificial dielectric unit cell.

3.2 Thickness of Ideal Artificial Dielectric Unit Cell

To achieve a specific required phase range, a schematic unit cell, like the one in Fig. 3.1(b), can be considered. This unit cell is assumed to be made of three sections: a central one referred to as the core, where the highest achievable effective permittivity $\varepsilon_{r,\max}$ is used to maximize the phase shift at the center of the lens, and two matching layer sections, responsible for the low-reflection transition to free space, over a desired bandwidth.

The highest achievable permittivity $\varepsilon_{r,\max}$ depends on the maximum frequency of operation, the minimum height of dielectric slabs (i.e. minimum inter-layer distance), and the minimum gap and track width of the manufacturing technology. The matching section design depends on the value of $\varepsilon_{r,\max}$ and on the desired operational bandwidth.

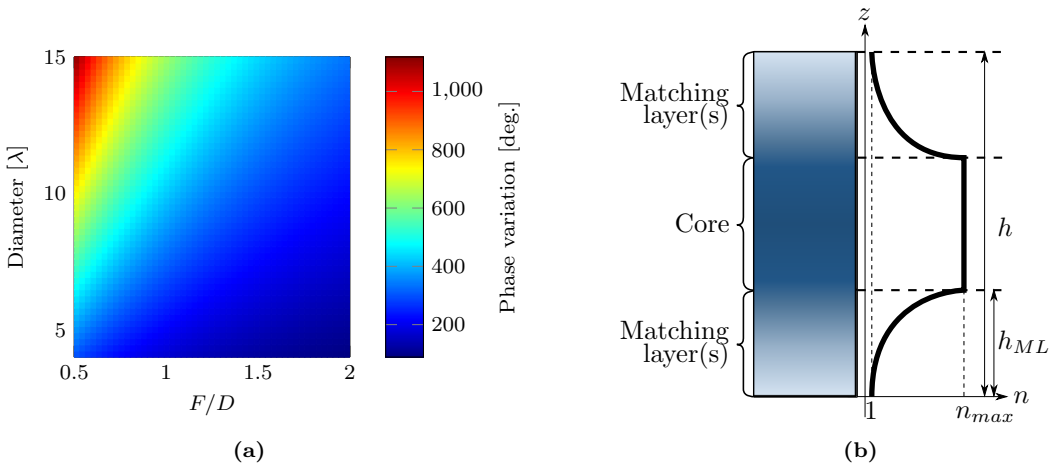

Figure 3.1: (a) Map of maximum phase variation in degrees for different values of lens diameter D and focal ratio F/D. (b) Schematic of unit cell. Core with refractive index $n_{\max}$, and matching layers with gradually reducing refractive index.

The schematic unit cell allows estimating the total phase shift that can be obtained with an ideal unit cell for a given $\varepsilon_{r,\max}$ and a certain total height h. For the sake of simplicity, we assume that the matching layers are realized as an exponentially tapered impedance transformer between free space and the core material [17]. For example, for the lower matching layer, we can write:

$$Z(z) = Z_{\mathrm{FS}} e^{az} \text{ for } 0 \leq z \leq h_{ML} \tag{3.1}$$

where Z_{FS} is the free-space impedance and a is

$$a = \frac{1}{h_{ML}} \ln\left(\frac{Z_{\mathrm{core}}}{Z_{\mathrm{FS}}}\right). \tag{3.2}$$

Writing Eq. (3.1) in terms of refractive index, we have

$$Z(z) = \frac{Z_{\mathrm{FS}}}{n(z)} = Z_{\mathrm{FS}} e^{az} \Rightarrow n(z) = e^{-az} \tag{3.3}$$

so that the phase shift of the matching layer with height h_{ML} can be found in closed form:

$$\phi = k_0 \int_0^{h_{ML}} n(z)dz = k_0 \int_0^{h_{ML}} e^{-az} dz = \frac{k_0(1 - e^{-ah_{ML}})}{a}. \tag{3.4}$$

The same phase shift can be assumed for the top matching layer. We assume that the amplitude of the reflection coefficient for an exponential taper can be approximated as [17]

$$|\Gamma| = \frac{1}{2} \ln\left(\frac{Z_{\mathrm{core}}}{Z_{\mathrm{FS}}}\right) \mathrm{sinc}(k_0 h_{ML}). \tag{3.5}$$

The height h_{ML} can be chosen such that the total reflection coefficient of the unit cell is better than a desired value over a target bandwidth. For example, we can choose $\Gamma \leq -13$ dB over a relative band $\geq 40\%$ (from $0.66f$ to f, where f is the maximum frequency of operation), which

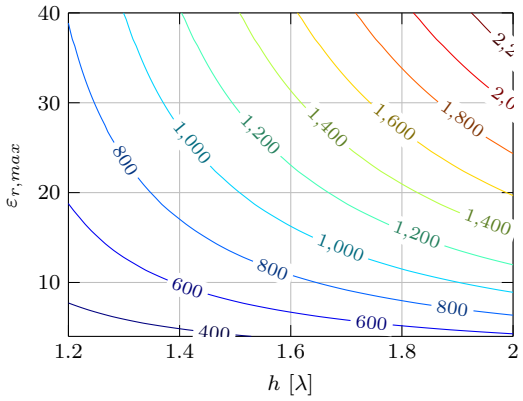

Figure 3.2: Maximum phase variation as a function of the maximum effective permittivity and total lens thickness, for a flat lens with a 40% bandwidth.

corresponds to a total reflection $\Gamma \leq -10$ dB for the two matching layers. These conditions define the matching section height h_{ML}, and in turn the height of the core section can be defined as $h_{core} = h - 2h_{ML}$. The map of maximum phase variation as a function of $\varepsilon_{r,\max}$ and h is shown in Fig. 3.2. For example, if a certain lens design requires 800° of phase range, one can use a material with relative permittivity of 30 for the core and obtain a lens thickness of 1.25λ. Alternatively, if the maximum permittivity that can be achieved is 10, a lens of 1.65λ height would be required to achieve the same phase shift. It can be seen that, with the considered high values of core permittivity, several multiples of 360° can be achieved even with moderate lens thicknesses between one and two wavelengths.

3.3 Technology Constraints

The value of $\varepsilon_{r,\max}$ is dependent on the manufacturing technology. The first step in the design is to determine the maximum effective permittivity, given the manufacturing technology. The permittivity is proportional to the spatial density of the metal patches. The constraints taken into account are the following:

- Minimum gap width between patches.
- Dielectric material for the lens.
- Minimum distance between patch layers, i.e. the minimum thickness of a dielectric slab.
- The period of the artificial dielectric layer has to be small compared to the wavelength at the maximum frequency. This condition is essential for keeping low current intensity on the patches and, in turn, low Ohmic losses. Moreover, the assumption of small patches is needed for the validity of the analytical descriptions of the ADL. The analytical expressions are typically valid for ADL periods lower than a quarter wavelength.

From these constraints, a hypothetical unit cell is designed with the minimum gap width between the patches, minimum vertical spacing d, maximal lateral shifts s between the metal layers, a small period p and using the selected dielectric as the host material. From this unit cell, the maximum effective refractive index is determined. The dimensions of this unit cell are used for the core of the unit cell in the center of the lens, to achieve the maximum possible phase shift.

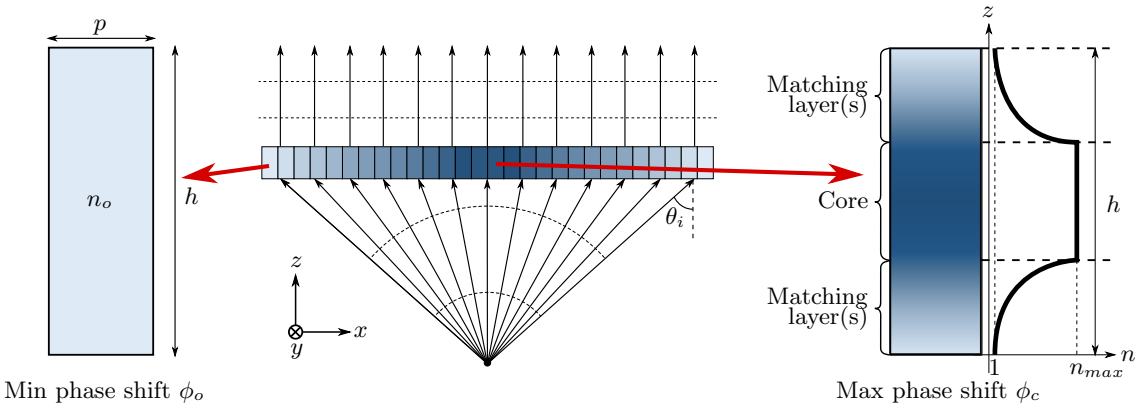

Figure 3.3: Overview of the lens divided into unit cells. In the center, the maximum phase shift is realized, gradually decreasing towards the lens's periphery.

3.4 Unit Cell Design

The lens is first designed assuming unit cells of homogeneous dielectrics. Later, these will be implemented as ADLs. Knowledge of the ADL period and possible constraints in thicknesses of the available dielectric layers are required. Both should be considered when determining the heights of the core and matching layers.

The first step of the lens design is the division of the lens into a number of unit cells, as depicted in Fig. 3.3. The period of these unit cells is the same as the period of the ADL. The unit cell in the center provides the maximum phase shift, and the outermost unit cell provides the minimum phase shift ϕ_o, considering the angle of incidence θ_i on this unit cell. Given the maximum phase variation ϕ_m for certain F/D, the center unit cell should provide a phase shift of

$$\phi_c = \phi_m + \phi_o \,. \tag{3.6}$$

The center position of each unit cell is used to compute the phase shift required in that particular cell, considering the angle of incidence of a plane wave originating in a point source in the focal point of the lens. Assuming that the focal point is in the origin of the coordinate system, the radial distance of a unit cell centered at (x, y) to the center of the lens is defined as $\rho = \sqrt{x^2 + y^2}$, and the angle of incidence on a unit cell is

$$\theta_i = \tan^{-1}\left(\frac{\rho}{F}\right) . \tag{3.7}$$

The maximum incidence angle for the unit cell at the edge of the lens can be found as

$$\theta_{max} = \tan^{-1}\left(\frac{D-p}{2F}\right) . \tag{3.8}$$

Assuming the outermost unit cell is made of a single homogeneous dielectric with refractive index n_o, phase shift through that unit cell is

$$\phi_o = -k_0 \cos\left(\theta_{max}\right) h n_o \,. \tag{3.9}$$

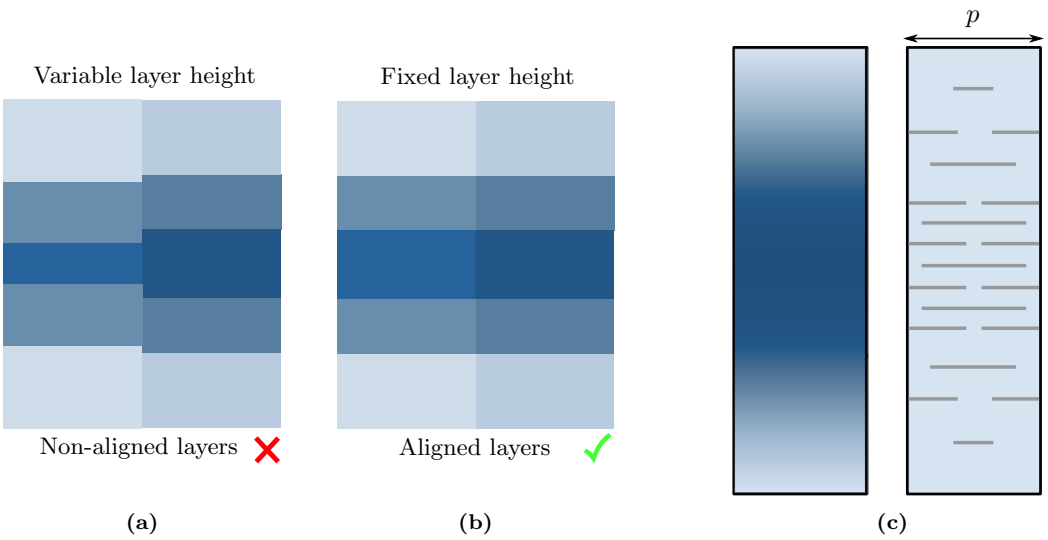

Figure 3.4: Drawing of (a) non-fixed layer heights of the core and matching layers, and (b) fixed layer heights to ensure the (metal) layers of the lens are aligned. (c) Conceptual synthesis of ADL from unit cell: higher metallic insertion density yields higher effective refractive index.

The target phase shift ϕ_t required for a unit cell at a distance ρ from the origin can be written in general as

$$\phi_t = -k_0 \left[\sqrt{\left(\frac{D-p}{2}\right)^2 + F^2} - \sqrt{(\rho^2 + F^2)} \right] + \phi_o \,. \tag{3.10}$$

Given a bandwidth requirement, one can design the matching layers of the center unit cell. The thickness of the core should be chosen to provide the proper phase shift. The center unit cell can be used as a starting point to design all other unit cells within the lens.

To find the permittivity of the core and matching layer(s) of any cell, the permittivity of the core can be varied from 1 to $\varepsilon_{r,\max}$ while changing the matching layer(s) accordingly. Computing the phase of S_{12} generates a map of the achievable phase shifts considering the angle of incidence on a given unit cell. The permittivity of the core and the matching layers for which the phase of the S_{12} is equal to ϕ_t are used in that particular unit cell. When considering different unit cells with different dielectric materials, both the height of the core and the height of the matching layers change, for optimal matching conditions. However, this would result in a complex structure that is difficult to manufacture because of the non-aligned interfaces between dielectrics, as shown in Fig. 3.4(a). For this reason, it is convenient to keep the same height of the matching layers for all unit cells so that the lens can be fabricated with a single multi-layer printed circuit board (PCB). Fig. 3.4(b) illustrates the fixed layer height. This constraint worsens the matching compared to the ideal transformer because the matching layers are no longer a quarter of the effective wavelength. However, small degradation of the reflection coefficient can still be acceptable.

The above procedure yields a height for the core and each matching layer. Furthermore, for each unit cell, an equivalent target permittivity is defined for the core and the matching layers(s). The problem of designing a flat lens has now essentially been reduced to a set of ADL synthesis problems, equivalent to the synthesis procedure described in Chapter 2.4. The dielectric sections are translated into a unit cell composed of ADLs, as shown in Fig. 3.4(c). The phase of the

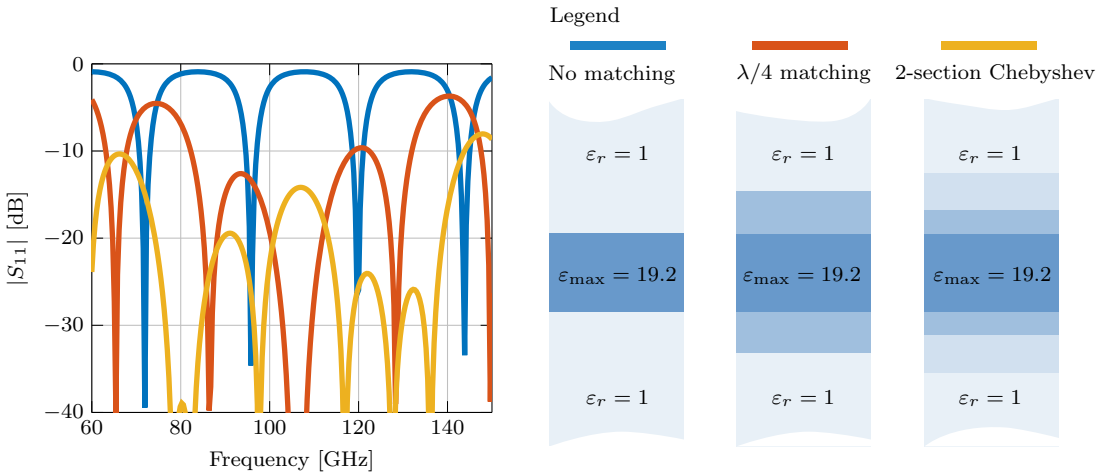

Figure 3.5: Reflections of a dielectric slab ($\varepsilon_r = 19.2$) with 0, 1 and 2 Chebyshev matching sections on above and below the slab.

unit cell's S_{12} is designed to be equal to ϕ_t while also considering the bandwidth requirements in terms of $|S_{11}|$.

In the next section, this theory will be applied to the design of an 11λ diameter flat lens with an operating bandwidth of an octave.

3.5 Example Flat Lens Design

This section details the design of a flat lens based on ADLs, using PCB technology. The target performance is summarized as follows:

- The operating frequency band is from $70-140$ GHz, over which a $|S_{11}| < 10$dB is required for each unit cell.
- The diameter of the lens is $11.6\lambda_0$, where λ_0 is the free-space wavelength at the maximum frequency, 140 GHz. This corresponds to a maximum directivity of 31dB.
- Focal number F/D =1.

The above requirements result in a maximum phase variation of 477° as can be derived from the map presented in Fig. 3.1(a).

The next step is to determine the maximum refractive index that can be achieved in a certain technology. The dielectric material for the lens is chosen as Rogers RO 4350B [22]. The chosen Rogers RO4350B PCB has the following properties and constraints:

- Minimum gap width between patches in PCB is 80 μm.
- Dielectric $\varepsilon_r = 3.66$ and $\tan\delta = 0.0037$.
- Minimum distance between patch layers is 101 μm.

Besides the material-related constraints, the period of the ADL is chosen as $0.19\lambda_0$, to ensure the low-loss property of the ADL and the validity of the analytical expressions. The maximum

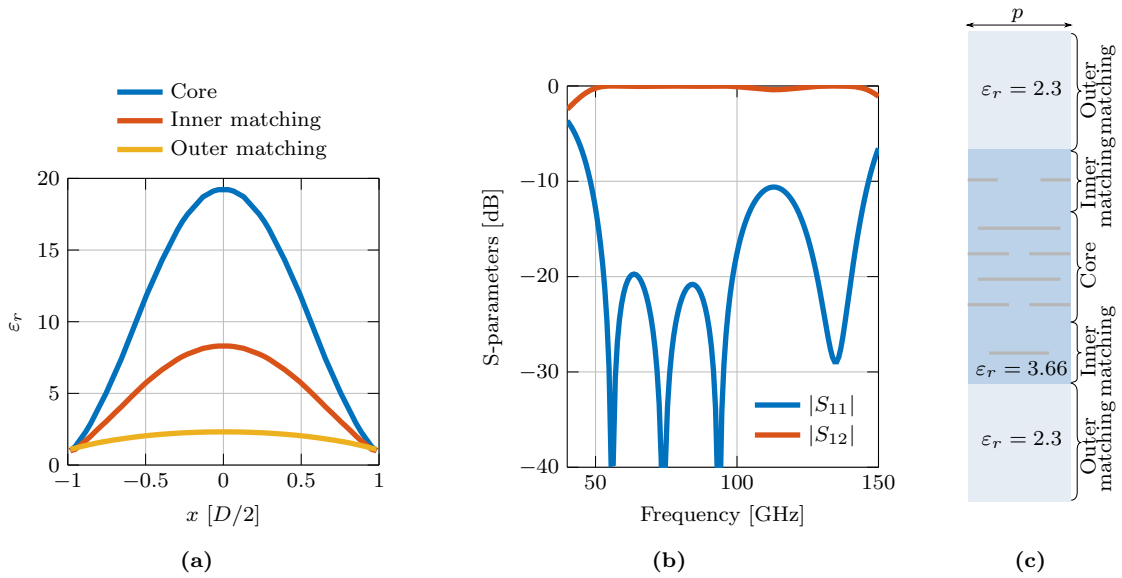

Figure 3.6: (a) Relative permittivity for the core, which is the densest, and the inner and outer matching layers. (b) Reflection coefficient S_{11} and transmission coefficient S_{12} of the center unit cell, implemented as ADL. (c) Schematic of the center unit cell. The core and inner layer are implemented using ADLs, the outer matching layer as a homogeneous dielectric.

achievable permittivity using these materials and constraints, is $\varepsilon_{r,\max} = 19.2$.

One can design the matching layer(s) with the maximum permittivity of the known core. A multi-section Chebyshev transformer was used in this particular design. One can investigate the reflection coefficient over the required frequency band to determine the number of sections required. The Chebyshev transformer is designed at the center frequency of operation, $f_c = 105$ GHz. In Fig. 3.5, the $|S_{11}|$ for a dielectric slab with $\varepsilon_r = 19.2$ and thickness of $\lambda_0/2$, with 0, 1 and 2 Chebyshev matching sections above and below the slab is plotted. Most power is reflected over the complete frequency band if no matching layers are used. As expected, periodic narrow transmission notches are observed, corresponding to resonances occurring when the core height is an integer multiple of half the effective wavelength. With one matching layer, the reflection coefficient is mostly lower than -10dB, but not over the entire target band 70-140 GHz. Adding a second matching layer yields a bandwidth < -10dB over the full band. More matching layers could be added to increase the bandwidth further or decrease the reflections in the pass band. This illustrates the trade-off between lens thickness and bandwidth.

With a 2-section Chebyshev transformer, a core thickness of 0.41 mm is sufficient to achieve the required total phase variation of 477° in the center of the lens. The total unit cell thickness is 1.8 mm, or $0.85\lambda_0$.

The thickness of the core, h_{core}, and of the matching layers h_1 and h_2 are fixed. For each cell, a curve similar to the one in Fig. 3.8(b) is created, considering the angle of incidence on that particular unit cell. This yields a permittivity for the core and the matching layers for each unit cell. In Fig. 3.6(a), the distributions of needed permittivities along the lens aperture are plotted. The core has the highest permittivity, and the matching layers have a lower permittivity. At some positions, the permittivity is lower than the permittivity of the host material. It is assumed those sections can be realized for now. Notes on the practical implementation can be found in

Chapter 6.

Now, the permittivities of each unit cell are known, and the remaining part is the ADL synthesis. The outer matching layer with low permittivity can be realized just with the dielectric and does not require metal insertions. Considering the constraints defined before, one can synthesize the unit cell that will be placed in the center of the lens. The realized unit cell has a reflection coefficient < 10dB over the entire bandwidth of operation, as can be seen in Fig. 3.6(b). The unit cell has 6 metal layers and is shown in Fig. 3.6(c). One thing to note is that if the F/D ratio

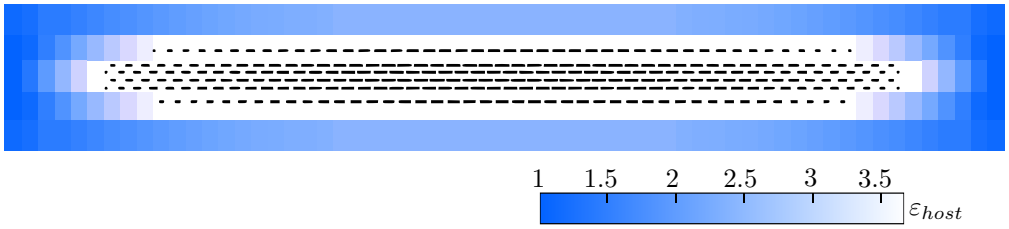

Figure 3.7: Cross-section of the flat lens with all unit cells designed.

was smaller, or D was larger, the required phase variation would be higher, but the matching layers could be realized in the same way. Considering the same constraints, this would result in a higher number of metal layers in the core to realize the required phase shift.

The unit cell at the center is used as a starting point to derive all other unit cells. Essentially altering the geometrical parameters of ADLs in the core to change the phase shift, and in matching layers to improve matching. A cross-section of the final lens design is shown in Fig. 3.7.

The reflection coefficient for all the unit cells under oblique incidence is shown in Fig. 3.8(a). It can be noted that some of the unit cells exhibit reflections slightly above -10dB. Although a better optimization could have been performed, the total losses due to reflection were estimated to be lower than 0.5 dB, and thus were considered acceptable for this example design.

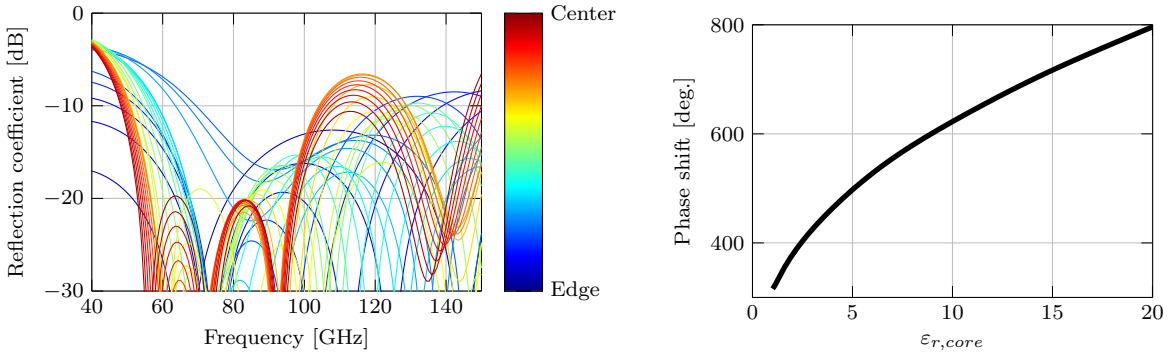

Figure 3.8: (a) Reflection coefficient over frequency for each of the unit cells in the lens design. The color indicates the radial position on the lens. (b) Phase shift achieved by a unit cell including matching layers for different core permittivities.

Chapter 4

Modeling of the Lens

This chapter presents a combined geometrical optics (GO) / physical optics (PO) approach for the evaluation of the lens' radiation patterns and efficiency. Each GO ray is studied as a plane wave problem to evaluate the lens's reflection/transmission through each unit cell. This method allows for quickly assessing the performance in terms of directivity of a flat lens based on artificial dielectric layers.

4.1 System Overview

The total system is composed of the following components:

- A feed, placed at a distance F from the lens. The feed can be displaced laterally from the focal point of the lens by distance d_f from the point O aligned with the lens axis. The line connecting the feed with the center of the lens forms an angle α with respect to the z-axis, while the line connecting with a generic point on the lens (with radial distance ρ for the center) forms an angle θ with respect to the z-axis.
- The lens with diameter D. In turn, the lens is defined by the geometry and stratification of each unit cell, characterized by a transmission coefficient that relates the incident and transmitted field, depending on the angle of incidence theta and the polarization of the incident field (TE or TM).

A schematic drawing of the system is given in Fig. 4.1. In the figure, the $\phi = 0$ cut is drawn. If there is no lateral feed displacement, the system is circularly symmetric, although the pattern of the feed is not necessarily symmetric. If there is a lateral feed displacement, this symmetry disappears.

4.2 Feed

To decouple the problem of designing a frequency-stable feed from the lens design, a Gaussian feed with -10dB edge taper was used to assess the lens performance. The design of a frequency-stable feed is out of the scope of this thesis. In Chapter 6.2 some feasible feed options are presented.

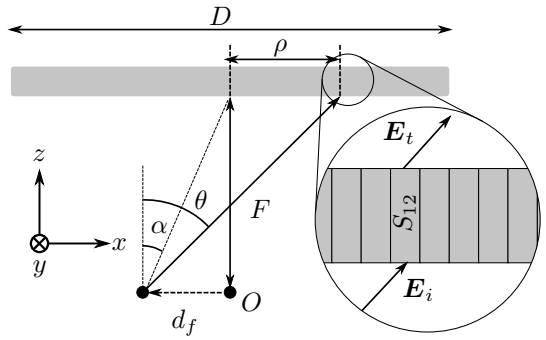

Figure 4.1: System overview.

4.2.1 Current Distribution

The feed current distribution is assumed to be planar in the x-y plane, and only an electric current along $\hat{\boldsymbol{x}}$. The Gaussian current distribution is given by

$$\boldsymbol{j}(\rho) = e^{-\rho^2/w_0^2}\hat{\boldsymbol{x}} \tag{4.1}$$

where ρ is defined as $\sqrt{x^2+y^2}$, and w_0 is a constant to scale the distribution. w_0 is chosen such that the far-field has a -10dB edge taper at the lens edge, and is frequency dependent. Since the field amplitude does not decay with the angle the same way in the E- and H-plane, the source current is stretched by substituting $y = y' = ya$, where a is a constant chosen to match the -10dB angles in both planes.

Because the current defined here will also be exported to a full-wave solver (CST), it is chosen to be sampled on a finite rectangular grid. Therefore, the Gaussian will be truncated. The same truncation is used in this analysis.

4.2.2 Beam Scanning

To achieve beam scanning with the lens, the feed is displaced laterally in the focal plane. This causes the illumination of the lens to change, resulting in degraded spillover- and taper-efficiency,

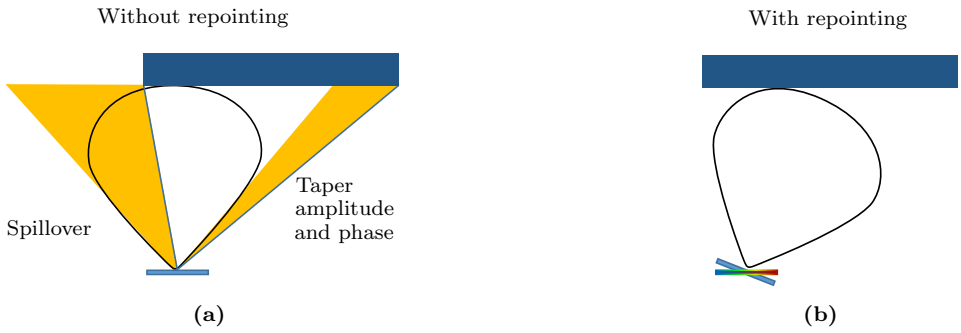

Figure 4.2: Scanning by lateral displacement in the focal plane, (a) without repointing and (b) with repointing.

as shown in Fig. 4.2(a). To partly compensate for this change in illumination, a linear phase shift is applied over the current distribution of the lens, resulting in a re-pointing of the beam of the feed to the center of the lens, as shown in Fig. 4.2(b).

Considering a displacement d_f of the feed along the x-axis, the angle α with the z-axis is defined as

$$\alpha = \tan^{-1}(d_f/F)\,. \tag{4.2}$$

The linear phase distribution over the feed aperture required to re-point the main lobe to the center of the lens, at angle α, is

$$\phi_\alpha(x) = k_0 \sin(\alpha)(x + d_f)\,. \tag{4.3}$$

The importance of this re-pointing becomes clear when one considers the scan loss curves of an example design with $F/D = 1$ in Fig. 4.3. The difference between both curves can be attributed mainly to the spillover and taper losses present when no re-pointing is used.

4.2.3 Far-field from Current

To find the far-field from the current distribution of the feed, the procedure described in Appendix B was used. The observation points are defined by the centers (x_l, y_l) of each unit cell on the lens bottom surface. The coordinates are transformed from Cartesian to spherical using

$$r = \sqrt{(x_l - d_f)^2 + y_l^2 + F^2} \tag{4.4}$$

$$\theta = \cos^{-1}\left(\frac{F}{r}\right) \tag{4.5}$$

$$\phi = \tan^{-1}\left(\frac{y_l}{x_l - d_f}\right) \tag{4.6}$$

Note that when computing ϕ, the four-quadrant inverse tangent should be used, which is available in MATLAB as `atan2()`.

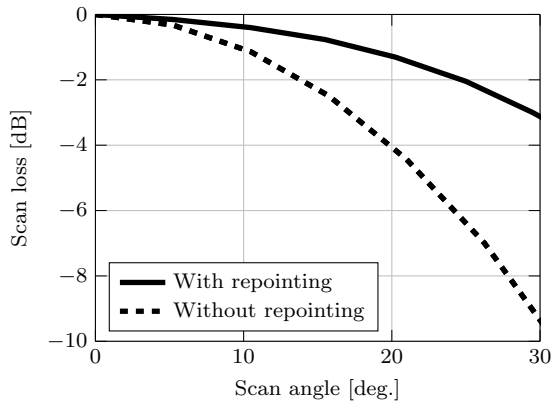

Figure 4.3: Scan loss for a lens with and without re-pointing of the feed main beam to the center of the lens.

4.3 Physical Optics Currents After Lens

As described in Section 2.2, artificial dielectric layers can be modeled as an equivalent transmission line with a plane wave impinging. This allows finding the S-parameters as a function of incident angle θ, frequency f, and polarization.

Note that the analytical expressions for the artificial dielectric layers are valid under the assumption of local periodicity, i.e., an infinitely repeating unit cell in both x- and y-direction. In Chapter 5 the implications of this assumption are investigated.

To find the transmitted E-field after the lens $\boldsymbol{E}_t$, the $\hat{\theta}$- and $\hat{\phi}$-components of the incident E-field before the lens $\boldsymbol{E}_i$ are multiplied by the S_{12} of the unit cell for respectively TM- and TE- mode.

$$\boldsymbol{E}_t = \boldsymbol{E}_{i,\theta} S_{12,TM} \hat{\boldsymbol{\theta}} + \boldsymbol{E}_{i,\phi} S_{12,TE} \hat{\boldsymbol{\phi}} \,. \tag{4.7}$$

With the E-field after the lens known, the equivalent Physical Optics surface currents after the lens are defined as

$$\boldsymbol{j}_s = \hat{n} \times \boldsymbol{H}|_s \tag{4.8}$$

$$\boldsymbol{m}_s = \boldsymbol{E}|_s \times \hat{n} \tag{4.9}$$

on the top surface after the lens. Using Schelkunoff's formulation of the equivalence theorem and the image theorem, and using $\hat{n} = \hat{z}$, the magnetic currents cancel, and the total equivalent electric current can be written as

$$\boldsymbol{j}_s = 2\hat{z} \times \boldsymbol{H}|_s = 2\hat{n} \times \left(\hat{k} \times \frac{\boldsymbol{E}}{\zeta} \right) \Bigg|_s \,. \tag{4.10}$$

From the equivalent current distribution after the lens, again, the procedure described in Appendix B is used to find the far-field radiation. However, now the observation points are chosen on a hemisphere, i.e. $r = \text{Const.}$, $\theta_f \in [0°, 90°]$ and $\phi_f \in [0°, 360°]$.

4.4 Efficiencies

To find the gain of the lens, losses should be considered. This analysis considers the reflection efficiency, taper efficiency, spillover efficiency, and Ohmic efficiency.

4.4.1 Spillover Efficiency

The spillover efficiency is a measure of how much power radiated by the feed is intercepted by the lens. It is defined by

$$\eta_{\text{spillover}} = \frac{\int_0^{2\pi} \int_0^{\theta_0} |\boldsymbol{E}_{\text{feed}}|^2 \sin\theta d\theta d\phi}{\int_0^{2\pi} \int_0^{\frac{\pi}{2}} |\boldsymbol{E}_{\text{feed}}|^2 \sin\theta d\theta d\phi} \,, \tag{4.11}$$

where θ_0 is the angle, looking from the feed center, until which the lens extends. In Fig. 4.2(a) the spillover efficiency is illustrated. The shaded part is the power not intercepted by the lens. Note that for scanning, θ_0 is a function of ϕ.

4.4.2 Reflection Efficiency

The reflection efficiency measures the fraction of power accepted by the lens relative to the power with which the lens is illuminated. For an arbitrary lens illumination, the reflection efficiency is a weighted sum of the incident power divided by the total incident power. The time average Poynting vector $\boldsymbol{S}_{av}$ for a plane wave is given by

$$\boldsymbol{S}_{av} = \frac{|\boldsymbol{E}|^2}{2\zeta}\hat{\boldsymbol{k}}\,. \tag{4.12}$$

The vector $\hat{\boldsymbol{k}}$ is a unit vector in the direction of propagation of the plane wave. Splitting the Poynting vector in the TE- and TM-components yields

$$\boldsymbol{S}_{TE} = \frac{|E_\phi|^2}{2\zeta}\hat{\boldsymbol{k}} \tag{4.13}$$

$$\boldsymbol{S}_{TM} = \frac{|E_\theta|^2}{2\zeta}\hat{\boldsymbol{k}}\,. \tag{4.14}$$

Multiplying the incident Poynting vector by the S-parameter S_{12} for TE- and TM-mode and taking the dot product with the normal yields the transmitted power P_T.

$$P_t = \iint_S (|\boldsymbol{S}_{TE}(x,y)||S_{12,TE}(x,y)|^2 + |\boldsymbol{S}_{TM}(x,y)||S_{12,TM}(x,y)|^2)\cos\theta(x,y)dxdy\,. \tag{4.15}$$

The total incident power is given by an integral over the surface at the bottom of the lens:

$$P_i = \iint \boldsymbol{S}_{av}(x,y)\cos\theta(x,y)dxdy\,. \tag{4.16}$$

Finally, the reflection efficiency can be written as

$$\eta_{\text{reflection}} = \frac{\iint (|\boldsymbol{S}_{TE}(x,y)||S_{12,TE}(x,y)|^2 + |\boldsymbol{S}_{TM}(x,y)||S_{12,TM}(x,y)|^2)\cos\theta(x,y)dxdy}{\iint \boldsymbol{S}_{av}(x,y)\cos\theta(x,y)dxdy}\,. \tag{4.17}$$

4.4.3 Ohmic Efficiency

Losses occur in the lens both in the dielectrics and on the metals. To estimate this efficiency, a full-wave simulation of the structure is performed in CST Microwave Studio [23], to extract the power radiated by the feed $P_{\text{feed}}$and the losses in the dielectrics, $P_{\text{loss, dielectric}}$, and on the metals $P_{\text{loss, metal}}$.

$$\eta_{\text{Ohmic}} = \frac{P_{\text{loss, dielectric}} + P_{\text{loss, metal}}}{P_{\text{feed}}\eta_{\text{spillover}}\eta_{\text{reflection}}}\,. \tag{4.18}$$

The term in the denominator consists of three parts: the power radiated by the feed, the spillover efficiency, measuring how much power from the feed is actually intercepted, and the reflection efficiency. The product of those measures yields the total power accepted by the lens.

4.4.4 Taper Efficiency

The taper efficiency measures how constant the phase and amplitude of the field after the lens are. The taper efficiency can be computed by comparing the achieved directivity to the maximum directivity from an aperture with constant amplitude and phase of the same size. A different

definition of the taper efficiency split into amplitude taper loss (ATL) and phase error loss (PEL) is given in [24]. The directivity from an aperture with constant amplitude and phase is

$$\mathrm{Dir}_{\max} = \frac{4\pi A}{\lambda^2} \tag{4.19}$$

where A is the area of the aperture.

The ATL is defined as

$$\mathrm{ATL} = \frac{\left(\iint |E| ds\right)^2}{A \iint |E|^2 ds} \,. \tag{4.20}$$

Since the phase after the aperture should not be constant when scanning, this must be considered when defining the phase error. In general, one can write

$$\mathrm{PEL}(\theta, \phi) = \frac{(1+\cos\theta)^2}{4} \frac{\left|\iint E e^{j\boldsymbol{k}\cdot\boldsymbol{r}'} ds\right|^2}{\left(\iint |E| ds\right)^2} \,. \tag{4.21}$$

For broadside, the PEL reduces to

$$\mathrm{PEL} = \frac{\left|\iint E ds\right|^2}{\left(\iint |E| ds\right)^2}. \tag{4.22}$$

With the ATL and PEL, the taper efficiency is defined as

$$\eta_{\mathrm{taper}} = \mathrm{ATL} \cdot \mathrm{PEL} \,. \tag{4.23}$$

4.5 Comparison with Full-Wave Simulations

To validate the analysis method, full-wave simulations were done using CST Mircrowave Studio [23]. In these simulations, the same -10dB edge-tapered feed was used. The *"Near-field scan data exchange format"* [25] was used to import the feed current distribution.

Furthermore, since the patches of the ADL can have shifts, a metal patch is not generally placed in the center of a unit cell. This can cause problems when two adjacent unit cells do not have the same gap width; since the metal patches vary in size from one to the other unit cell, very small and difficult to mesh features appear at the edges of the metal layers, resulting in simulations that are computationally too heavy. Therefore, the jump from one to the next unit cell was made to vary linearly, reducing the number of mesh cells significantly in the simulations and improving convergence. In Fig. 4.4, a schematic drawing of this conversion is given.

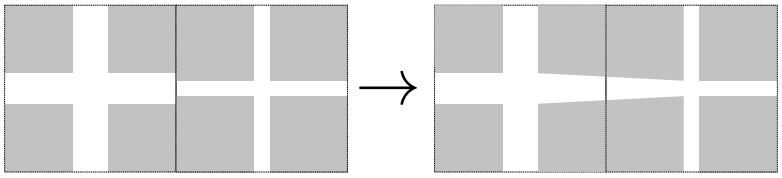

Figure 4.4: Schematic of conversion from square patches to taper for full-wave simulations.

4.5.1 Example: F/D = 1 Design

The example design from Chapter 3.5 was analyzed using the GO/PO method described in this chapter. In Fig. 4.5 the far-field patterns of the flat lens illuminated by a -10dB edge-tapered Gaussian beam at 140 GHz are shown. The estimate of the maximum directivity, as well as the shape of the main beam, computed using the GO/PO method is very close to the results from the CST simulation. As the lateral displacement of the feed is increased, and thus the scan angle of the main beam, some small differences between CST and the GO/PO method start to emerge. However, the GO/PO method can still be used as an excellent estimate for the directivity.

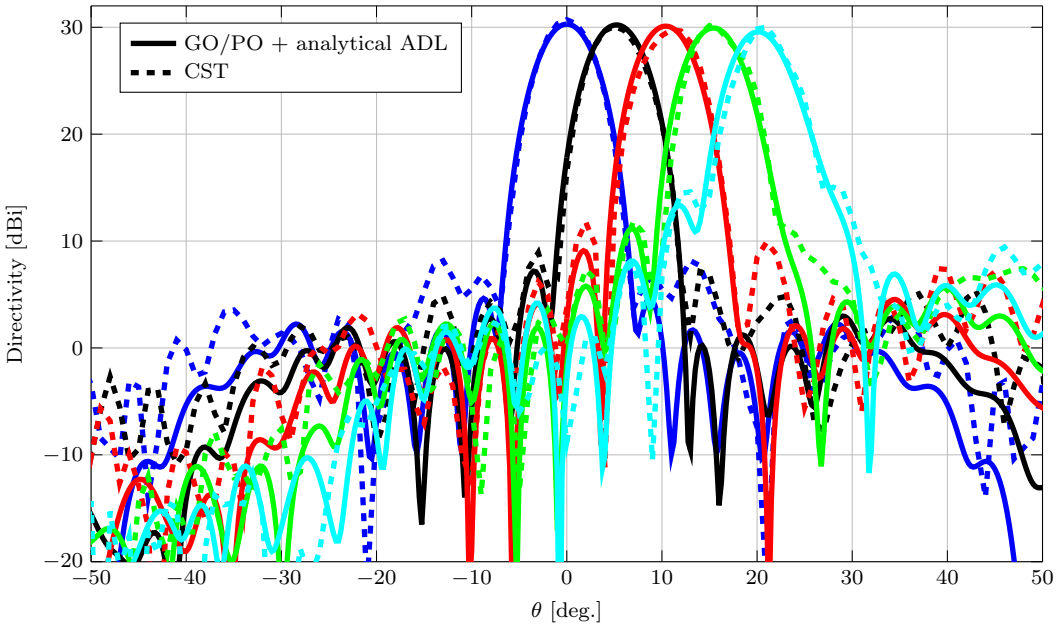

Figure 4.5: Directivity at 140 GHz of the flat lens design described in Chapter 3.5, for different lateral displacements of the feed.

To estimate the gain and total efficiency, the different efficiencies were computed for this particular design. An overview of the efficiencies as a function of frequency is presented in Fig. 4.6(a). The total efficiency over an octave bandwidth is higher than -2dB or 63%. As the frequency increases, one can observe that the Ohmic losses increase, as the electrical size of the metal patches grows. Furthermore, the reflection losses dip at 120 GHz. This was expected, as at this frequency the reflection coefficients of some individual unit cells (as reported in Chapter 3.5), exceeded the targeted −10dB level.

The maximum achievable directivity for this design was 31dB at 140 GHz. In Fig. 4.6(b), the achieved gain for broadside is plotted, along with the maximum achievable directivity for a circular aperture the size of the lens. The achieved gain at 140 GHz is 29.3dB.

As can be seen in Fig. 4.5, the maximum directivity is reduced as the scan angle increases. The scan loss for this lens at 140 GHz is plotted in Fig. 4.7(a). When scanning up to 25°, the scan loss is lower than −2dB.

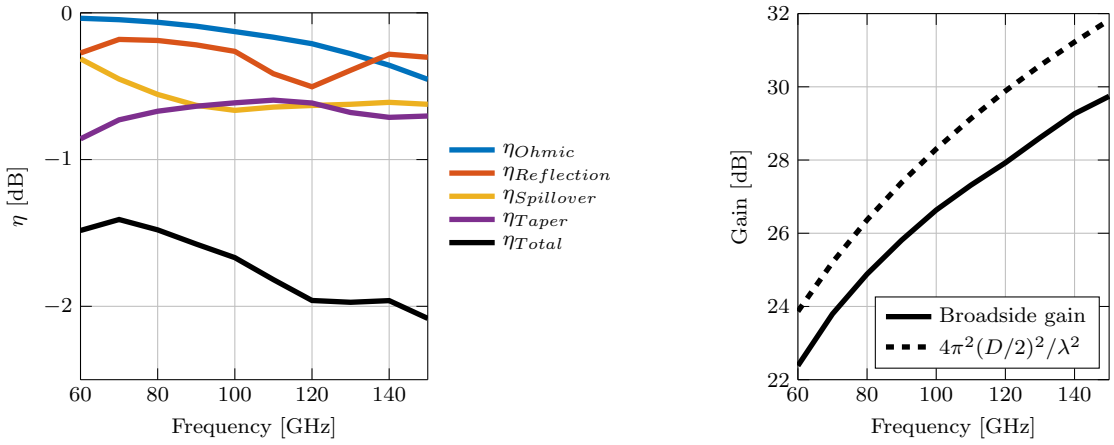

Figure 4.6: (a) Total efficiency and the contributions of each of the considered efficiencies: Ohmic, reflection, spillover, and taper efficiency. (b) Gain of the lens design (solid) and maximum directivity from an aperture (dashed).

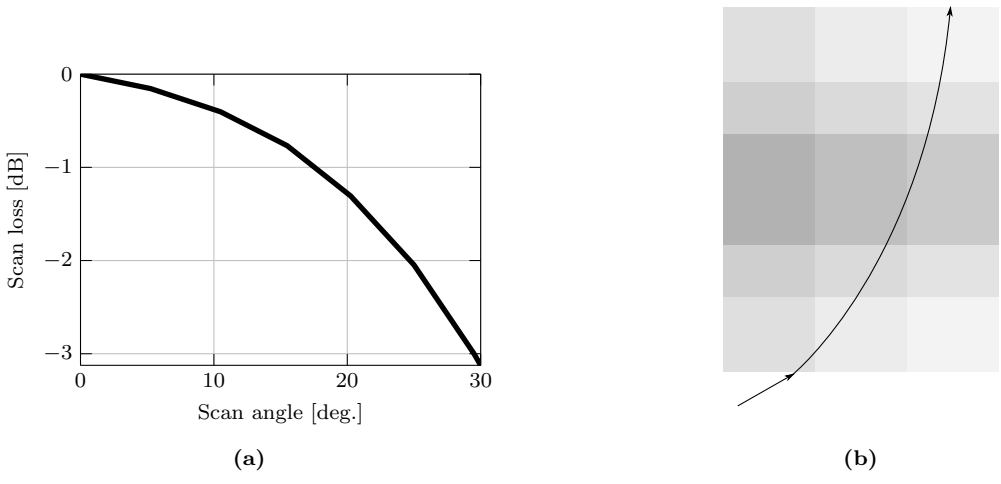

Figure 4.7: (a) Scan loss at 140 GHz. Until 25 degrees, the scan loss is limited to -2 dB. (b) A ray propagating through multiple unit cells.

4.6 Reduced F/D

When the F/D ratio is reduced, the maximum incident angle on the lens increases. If one applies the GO/PO analysis on a lens with a similar unit cell period and lens thickness in terms of the wavelength but reduced F/D, the shortcomings of this analysis become apparent. Consider the far-field pattern of a flat lens with $F/D = 0.25$ computed using the GO/PO method, compared to the full-wave simulations presented in Fig. 4.8. The main-beam shape is different; therefore, the estimate of maximum directivity for broadside is also more than 1 dB different.

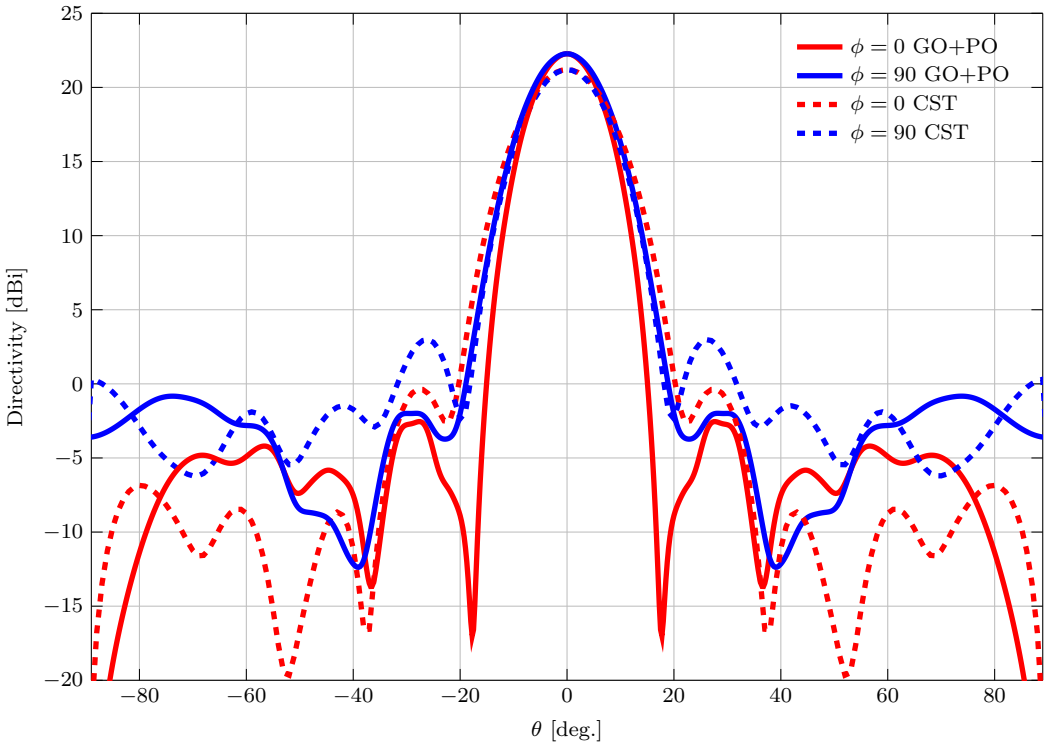

Figure 4.8: Far-field pattern from flat lens with $F/D = 0.25$, from CST [23] (dashed) and using the GO/PO method without raytracing (solid).

A reason for this mismatch between the simulation methods could be that in the GO/PO method, the unit cell on which a plane wave impinges is assumed to be locally periodic. This assumption is correct if a ray impinging on a unit cell remains within the same unit cell. However, if a ray traverses multiple unit cells, as shown in Fig. 4.7(b), this assumption is no longer valid, causing an error in the estimated field after the lens and thus the far-field pattern. The phenomenon in which rays traverse multiple unit cells depends of course on the period of the unit cells and thickness of the lens, but in general, as the feed is displaced more, or the F/D ratio is reduced, the number of rays that traverse multiple unit cells increases, as the incident angle on the unit cells increases.

In the next chapter, a method to model this phenomenon is proposed and applied to both the analysis and design of flat lenses.

Chapter 5

Ray Propagation in Non-Homogeneous Media

The analysis and design presented in the previous chapters assumed an incident ray is transmitted through a locally periodic unit cell. In reality, the properties of the lens vary spatially, and a ray arriving at the lens with an oblique angle can propagate through multiple unit cells that are different from each other. This effect can happen when the F/D ratio is small, causing the incident angle to be large in the periphery of the lens. When the feed is displaced significantly off-axis, the maximum incident angle on unit cells also increases.

The goal of this chapter is to provide the tools required to analyze rays propagating in non-homogeneous structures and use this to improve the lens design and analysis.

5.1 Ray Propagation in Non-Homogeneous Media

In non-homogeneous media, in which the index of refraction varies as a function of space, ray paths are not generally straight. For a special case in which the index of refraction is constant, i.e. in homogeneous media, ray paths are straight. For that case, the plane-wave solutions of the Maxwell equations in a homogeneous medium are:

$$\begin{aligned} \boldsymbol{E}(\boldsymbol{r}) &= \boldsymbol{E}_0 e^{-jk_0 n(\hat{\boldsymbol{k}}\cdot\boldsymbol{r})} \\ \boldsymbol{H}(\boldsymbol{r}) &= \boldsymbol{H}_0 e^{-jk_0 n(\hat{\boldsymbol{k}}\cdot\boldsymbol{r})}\,. \end{aligned} \tag{5.1}$$

where $n = \sqrt{\mu_r \varepsilon_r}$ is the refractive index, k_0 is the vacuum wavenumber, $\hat{\boldsymbol{k}}$ is the unit vector along the propagation direction and $\boldsymbol{r}$ is the position vector. If instead of defining the phase as a distance along the direction of propagation multiplied by the index of refraction, one defines a function $S(\boldsymbol{r})$, called the "optical path", and substitutes this for $n(\hat{\boldsymbol{k}} \cdot \boldsymbol{r})$, one can infer that a more general wave propagating far away (many wavelengths) from the sources can be represented by

$$\begin{aligned} \boldsymbol{E}(\boldsymbol{r}) &= \boldsymbol{E}_0 e^{-jk_0 S(\boldsymbol{r})} \\ \boldsymbol{H}(\boldsymbol{r}) &= \boldsymbol{H}_0 e^{-jk_0 S(\boldsymbol{r})}. \end{aligned} \tag{5.2}$$

If one substitutes these functions as trial solutions in the Maxwell equations, one can find the Eikonal equation. In Appendix C the full derivation is given. The Eikonal equation governs ray-propagation in non-homogeneous media and can be written as:

$$(\nabla S)^2 = n^2. \tag{5.3}$$

By manipulating the Eikonal equation following the algebraic steps also shown in Appendix C, one can arrive at two differential equations:

$$n\frac{d\boldsymbol{r}(s)}{ds} = \nabla S \tag{5.4}$$

and

$$\frac{d}{ds}\left(n\frac{d\boldsymbol{r}(s)}{ds}\right) = \nabla n\,. \tag{5.5}$$

One can derive an ordinary differential equations (ODE) system to solve these equations. Writing Eq. (5.4) in terms of its different components explicitly

$$n\frac{dx}{ds}\hat{\boldsymbol{x}} + n\frac{dy}{ds}\hat{\boldsymbol{y}} + n\frac{dz}{ds}\hat{\boldsymbol{z}} = \frac{\partial S}{\partial x}\hat{\boldsymbol{x}} + \frac{\partial S}{\partial y}\hat{\boldsymbol{y}} + \frac{\partial S}{\partial z}\hat{\boldsymbol{z}} \tag{5.6}$$

and defining $p_x = \frac{\partial S}{\partial x}$, $p_y = \frac{\partial S}{\partial y}$ and $p_z = \frac{\partial S}{\partial z}$, yields 3 scalar equations.

$$n\frac{dx}{ds} = p_x \tag{5.7a}$$

$$n\frac{dy}{ds} = p_y \tag{5.7b}$$

$$n\frac{dz}{ds} = p_z \tag{5.7c}$$

Similar for Eq. (5.5), one can write explicitly

$$\frac{d}{ds}\left(n\frac{dx}{ds}\right)\hat{\boldsymbol{x}} + \frac{d}{ds}\left(n\frac{dy}{ds}\right)\hat{\boldsymbol{y}} + \frac{d}{ds}\left(n\frac{dz}{ds}\right)\hat{\boldsymbol{z}} = \left(\frac{\partial n}{\partial x}\hat{\boldsymbol{x}} + \frac{\partial n}{\partial y}\hat{\boldsymbol{y}} + \frac{\partial n}{\partial z}\hat{\boldsymbol{z}}\right). \tag{5.8}$$

Using Eq. (C.26), 3 scalar equations can be written:

$$\frac{dp_x}{ds} = \frac{\partial n}{\partial x} \tag{5.9a}$$

$$\frac{dp_y}{ds} = \frac{\partial n}{\partial y} \tag{5.9b}$$

$$\frac{dp_z}{ds} = \frac{\partial n}{\partial z} \tag{5.9c}$$

The combination of Eq. (C.26) and Eq. (C.28) yields the full ODE system. To solve it, a numerical solver can be used to solve the initial value problem, where the initial values are given by

$$x = x_0 \tag{5.10a}$$

$$y = y_0 \tag{5.10b}$$

$$z = z_0 \tag{5.10c}$$

$$p_x = n(x_0, y_0, z_0)\sin\theta\cos\phi \tag{5.10d}$$

$$p_y = n(x_0, y_0, z_0)\sin\theta\sin\phi \tag{5.10e}$$

$$p_z = n(x_0, y_0, z_0)\cos\phi \tag{5.10f}$$

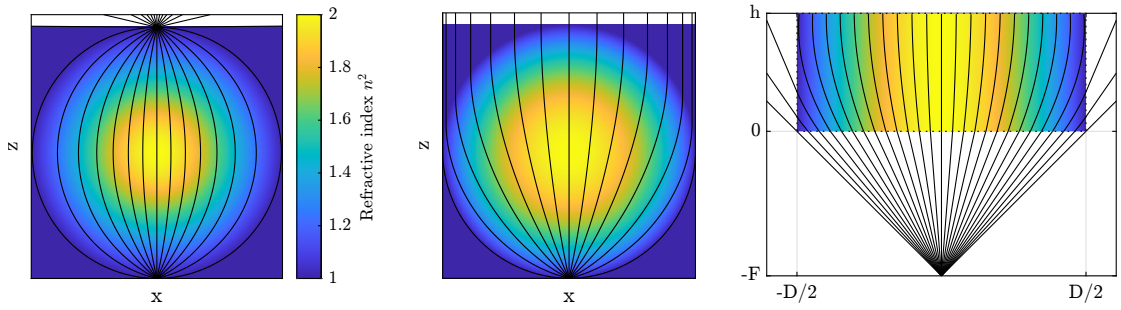

(a) **(b)** **(c)**

Figure 5.1: Ray paths in a (a) Maxwell fish-eye lens ($n_0^2 = 2$), (b) Luneburg lens and (c) the GRIN lens described in [27].

Numerical solvers, such as the `ode45` solver from MATLAB can be used to solve such problems.

The Eikonal equation is valid if the refractive index in the medium is slowly varying. Using the Eikonal equation and Snell's law at planar interfaces, ray propagation through complex structures with non-homogeneous materials and flat interfaces can be analyzed.

5.2 Testing Implementation of Eikonal Equation

To confirm the correctness of the implementation of the Eikonal equation and the ODE system, ray propagation in different lenses with known propagation characteristics is investigated.

Luneburg Lens and Maxwell Fish-Eye Lens: A famous example of a lens with a non-constant refractive index is the Maxwell fish-eye lens [26]. The Maxwell fish-eye lens is a spherical lens with a radius R. It focuses rays originating at a point on the sphere to the opposite side of the sphere. The refractive index n as a function of the distance from the center is

$$n = \frac{n_0}{1 + \left(\frac{r}{R}\right)^2}, \tag{5.11}$$

where n_0 is the maximum refractive index. A 2D cut of such a lens with a source placed at the bottom is given in Fig 5.1(a).

Another example is the Luneburg lens. It focuses incident parallel rays onto a point on the opposite side of the lens. The refractive index n as a function of the distance from the center is

$$n = \sqrt{2 - \left(\frac{r}{R}\right)^2}. \tag{5.12}$$

In Fig. 5.1(b), the ray paths inside the Luneburg lens are plotted.

Graded Index (GRIN) Lens Example: Another example of a GRIN lens on which ray tracing was applied, is presented in [27]. The lens presented is a flat lens with a refractive index n as a function of ρ, varying as

$$n = n_{\max} + (n_{\max} - n_{\min}) \left(\frac{\rho}{\rho_{\max}}\right) \tag{5.13}$$

In the example, $n_{\max} = 1.44$, $n_{\min} = 1$, $h = 14.7$ mm, $D = 36$ mm, $F = D/2$. The ray paths are plotted in the example lens in Fig. 5.1(c). The ray paths are the same as given in the paper.

5.3 GRIN Lens Design Equation

For a lens that converts a spherical wavefront into a planar wavefront, [28] presents a closed-form expression for the variation of n with position. It is assumed that in the center of the lens the refractive index is maximal, $n = n_{\max}$. The goal is to have the same phase delay or optical path length from the focal point to the transmit point of the lens for each ray:

$$F + n_{\max}T = OP_1 + \int_{P_1}^{P_2} nds. \tag{5.14}$$

where F is the focal length, T is the thickness of the lens, O is the focal point, P_1 is the point on the lens interface and $\int_{P_1}^{P_2} nds$ is the optical path length (OPL): the refractive index integrated over the ray path. Note that to find the phase shift of a ray with wave number k along a ray path is OPL$\cdot k$, similar to the homogeneous case where the phase shift is the product of the physical length, index of refraction, and k.

Under certain assumptions, the integral for the optical path length can be closed, and the optical path length can be written in closed form as shown in [28], which yields

$$\int_{P_1}^{P_2} nds = \frac{T(3n_1^2 - 2\sin^2\theta)}{3\sqrt{n_1^2 - \sin^2\theta}}\,. \tag{5.15}$$

Combining this result with (5.14), one can write

$$F + n_{\max}T = \frac{F}{\cos\theta} + \frac{T(3n^2 - 2\sin^2\theta)}{3\sqrt{n^2 - \sin^2\theta}}\,. \tag{5.16}$$

5.3.1 Refractive Index Profile

The first step to a practical design is determining the thickness T given the maximum refractive index $n_{\max}$, or equivalently find $n_{\max}$ given T. To do so, θ is replaced with $\theta_{\max}$ and n is replaced with $n_{\min}$ in (5.16):

$$F + n_{\max}T = \frac{F}{\cos\theta_{\max}} + \frac{T(3n_{\min}^2 - 2\sin^2\theta_{\max})}{3\sqrt{n_{\min}^2 - \sin^2\theta_{\max}}}\,. \tag{5.17}$$

In the equation above is $n_{\min}$ the minimum refractive index in the lens and $\theta_{\max}$ the incident angle at the edge of the lens and given by

$$\theta_{\max} = \tan^{-1}\left(\frac{D}{2F}\right)\,. \tag{5.18}$$

In (5.17), T is the only unknown. This equation can be solved to find T.

Now, one can substitute T in (5.16) and solve the resulting equation to find the refractive index as a function of incident angle, which can be mapped to a position directly.

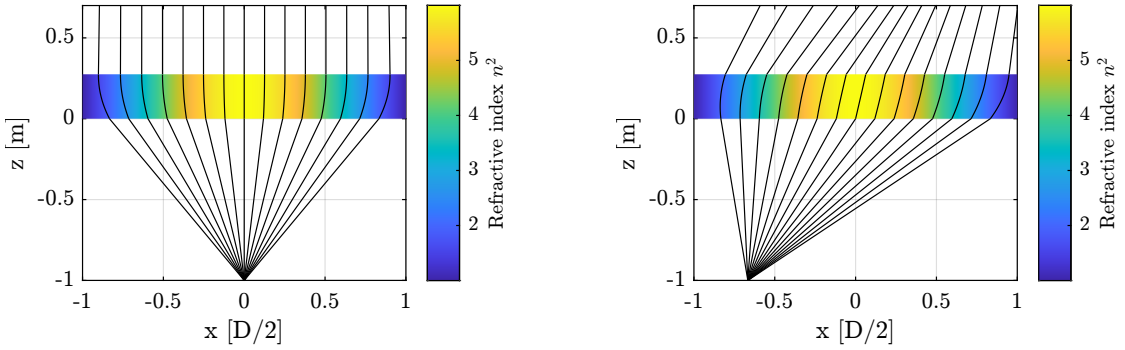

Figure 5.2: GRIN Lens with $F/D = 0.5$, designed using the method described in [28]. (a) Broadside rays. Most rays are parallel. (b) Rays when scanning. Since the lens was designed for broadside, not all transmitted rays are parallel.

5.3.2 Example GRIN Lens Design

Applying this design equation with $F/D = 0.5$, $n^2_{\text{max}} = 6$, $n^2_{\text{min}} = 1$ gives a GRIN lens design with thickness $T = 0.1375D$. In Fig. 5.2(a), the design, together with rays from a point source in the focal point is shown. The transmitted rays are parallel. Fig. 5.2(b) shows the same lens, but with the feed displaced. It can be noted that the transmitted rays are not all parallel, because the lens was designed for an on-axis feed.

5.4 Matching Layers

In the design equation presented in the previous section, the reflection of power incident on the lens was not considered. However, especially when the GRIN lens is designed with a large maximum refractive index to reduce its thickness, the incident field from the source can undergo strong reflection at the lens-air interfaces. To reduce this reflection, matching layers can be employed at the lens interfaces [8]. The procedure to close the integral of the optical path length cannot be used in the presence of matching layers, for which the refractive index also varies along z. Nevertheless, since the Eikonal equation is valid for arbitrary continuous refractive index distributions, the numerical procedure described in Section 5.1 can still be used when matching layers are included to compute the ray path.

5.4.1 Exponential Transformer

As an example implementation of a wideband matching layer, we consider an exponential transformer above and below the GRIN lens design from Section 5.3.2, now referred to as the core. The impedance of the transformer of length L is given by

$$Z(z) = Z_0 e^{az}, \tag{5.19}$$

where $a = \frac{1}{L} \ln \frac{Z_L}{Z_0}$. Since the lens dimensions and the refractive index profile changed, so will the ray paths. In Fig. 5.3(a) the ray paths are shown. L is chosen half of the core thickness. The transmitted rays are not parallel, and all rays are bent inward. The lens is over-compensating. A simple way to readjust the focusing property of the lens would be to reduce the thickness of

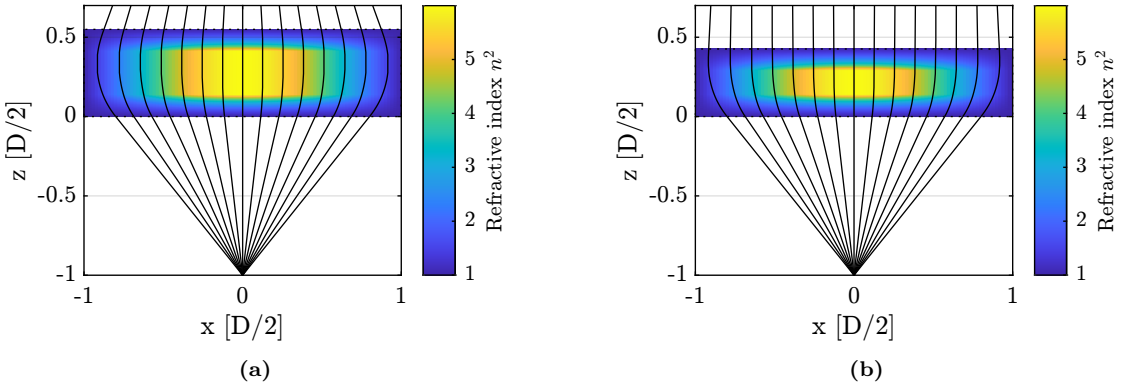

Figure 5.3: GRIN Lens with $F/D = 0.5$, designed using the method described in [28] with exponential matching layers. (a) Result after adding the matching layers. (b) Result after reducing the thickness of the lens core.

the core, but leave the matching layers unchanged. By reducing the core thickness to 55% of its original thickness, the transmitted rays are almost straightened, as can be seen in Fig. 5.3(b).

5.4.2 Arbitrary Transformers

For an arbitrary (discrete) transformer, there is no guarantee the rays can be straightened by changing the thickness of the lens and/or the thickness of the matching layer(s). Changing the refractive index profile in either the core or in one or multiple matching layer(s) might be necessary. This could be done for example with a correction of the refractive index profile described as a polynomial expansion with unknown coefficients that can be estimated with an optimization procedure.

5.5 Effective Refractive Index in ADL

The generalization of the ray propagation method in general media that are both inhomogeneous and anisotropic is much more complicated and requires cumbersome techniques like in [29], [30]. However, for the specific case of ADLs, the effective refractive index is a known function of the angle inside the structure. With the closed-form expressions of the refractive index inside the ADL as a function of angle, such as the one derived in Section 2.3.2, the refractive index inside the lens can be modelled as $n(\boldsymbol{r}, \theta)$, as in Eq. (2.39), Eq. (2.40) and Eq. (2.47).

Using this, arbitrary refractive index profiles can now be modified for use in the ODE system, taking into account the anisotropic effects of an ADL.

In Fig. 5.4, ray propagation in a GRIN lens with and without considering the anisotropic properties of ADLs is plotted. The transmit angle from Snell's law is altered at the first interface since the refractive index is altered. Throughout the lens, the propagation path is also different.

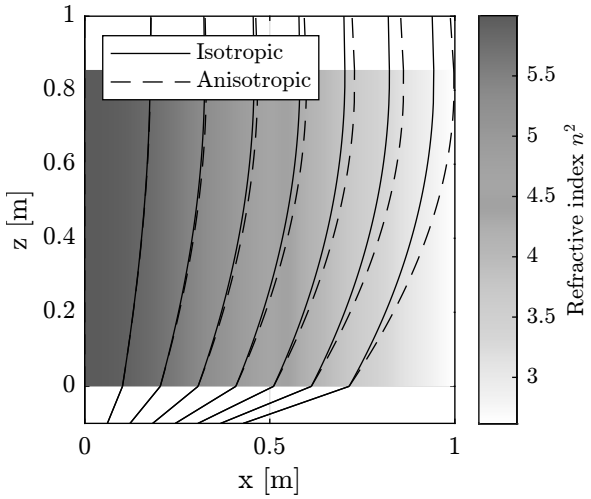

Figure 5.4: Ray propagation in GRIN lens with (dashed line) and without (solid line) anisotropic effects of ADLs, assuming TM polarization.

5.6 Ray Tracing in Lenses Designed Assuming Local Periodicity

In the design procedure outlined in Section 3.5, the phase shift through a unit cell was computed assuming the unit cell was locally periodic.

Under this assumption, each unit cell is designed to obtain a constant output phase distribution after the lens. However, if some rays propagate through multiple unit cells, the design assuming local periodicity gives some error in the phase distribution after the lens.

In Fig. 5.5, three examples of lenses designed with the method from Section 3.5, i.e. assuming local periodicity and discrete matching layers are shown. In Fig. 5.5(a), a lens with $F/D = 1$ is considered. The transmitted rays are almost parallel. As F/D decreases, for example to $F/D = 0.5$ in Fig. 5.5(b), the rays at the edges of the lens start diverging outward. If F/D is decreased to 0.25 in Fig. 5.5(c), this effect is even more pronounced. For the three cases, the transmit angles, the angle between the transmitted ray and the normal of the lens, are plotted in Fig. 5.6. In a perfect design, all transmitted rays are parallel to the normal of the lens.

Considering this, the design procedure outlined in Section 3.5 can give good designs, as long as the rays do not propagate through multiple unit cells. However, if the ray tracing shows skewed transmitted rays, this should be addressed to obtain a better design.

5.7 Designing a Small F/D Lens

To design a lens with a small F/D, for example, 0.25, the ray propagation through multiple unit cells should be considered to design the phase shift accurately. Besides the phase shift, the reflections must be considered for a practical lens design. Unfortunately, Eq. (5.16) cannot be used to design a lens with matching layers, since closing the integral of the optical path length requires a constant refractive index in the z (vertical) direction. The design procedure described in Section 3.5 does consider the reflections, and for a design with $F/D = 0.25$, this can be used

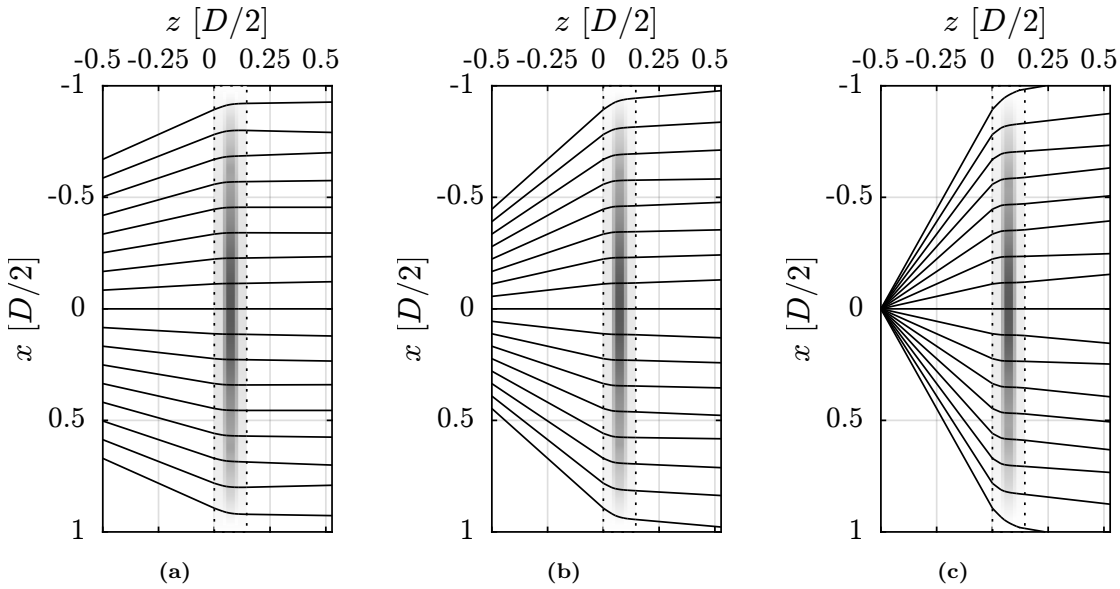

Figure 5.5: Ray propagation through flat lens based on artificial dielectric layers. (a) $F/D = 1$, the rays do not cross multiple unit cells. (b) $F/D = 0.5$, the transmitted rays are not all parallel. (c) $F/D = 0.25$, most transmitted rays are not parallel.

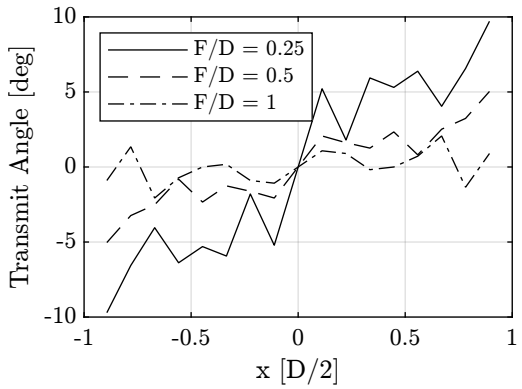

Figure 5.6: Transmit angles for rays propagated through three lenses, $F/D = 1$, $F/D = 0.5$ and $F/D = 0.25$, designed assuming local periodicity. As the F/D decreases, the transmit angles become larger.

as a starting point for the lens design considering the propagation through multiple unit cells.

The parameters for the design are summarised in Table 5.1.

Taking the refractive index profile as a starting point, and considering $n^2_{\text{host}} = 3.66$, the ray paths in the lens are plotted in Fig. 5.7(a). To improve this design, one can plot the transmit angles, and notice that the transmit angle is proportional to the derivative of the refractive index. A first-order approximation to the transmit angle is a linear variation, as can be seen in Fig. 5.7(b). The linear variation implies a quadratic compensation should be applied to the refractive index

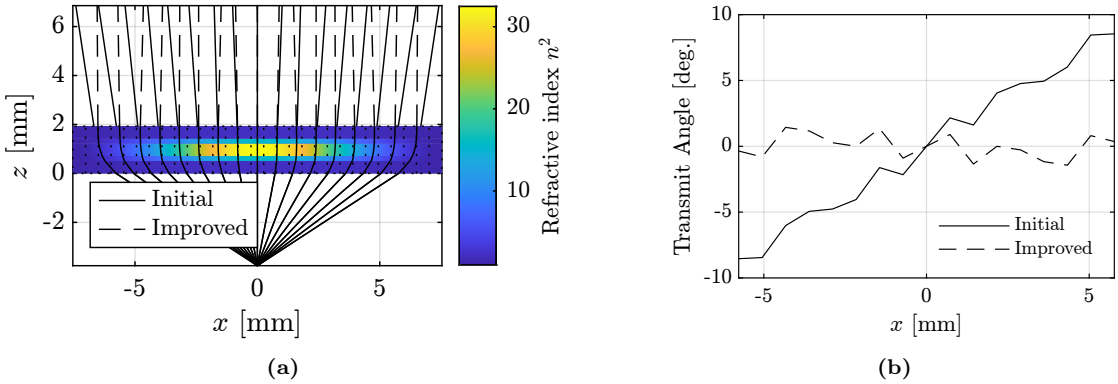

(a) (b)

Figure 5.7: (a) Ray paths in the flat lens before (solid lines) and after (dashed lines) corrections. (b) Angle between transmitted ray and lens normal, before (solid line) and after (dashed lines) corrections.

as a function of position:

$$n_{\text{new}} = n_{\text{old}} + ax^2 + b \tag{5.20}$$

where a and b are constants that can be estimated using an optimization technique.

Applying this correction to the inner matching layer and the core yields a new curve for the refractive index as a function of position for each layer, the improved design. As can be seen in Fig. 5.7(a), the ray paths are more parallel, which is also confirmed in Fig. 5.7(b). From this point, the ADL can be synthesized. The new refractive indexes sampled at each unit cell center are used as the target to which the phase should be matched. This can now be done for arbitrary plane-wave incidence, for example from broadside.

To actually see if the design yielded with this ray tracing method improves with respect to the design assuming local periodicity, simulations of both the initial design and the improved design were done using CST [23]. Since the −10dB edge-tapered Gaussian feed has an amplitude taper towards the edges of the lens, and most effects happen in the lens edges, a short dipole is used as feed to achieve a more constant illumination, to better highlight the effect of the improved lens design.

The resulting far-field at the maximum operating frequency in the E-plane is plotted in Fig. 5.8(a). The main beam of the initial design is significantly wider, causing the directivity to be around 1 dB lower for the initial design compared to the improved design at the highest frequency.

Table 5.1: Properties of flat lens design with $F/D = 0.25$.

Operating band	$75 - 110$GHz	
ADL Period	0.52 mm	$0.191\lambda_0$
Diameter	15.08 mm	$5.529\lambda_0$
Focal Length	3.77 mm	$1.382\lambda_0$
F/D	0.25	
$\theta_{in,max}$	63.4°	
Phase variation	585°	
# unit cells	29	
Thickness	1.93 mm	$0.71\lambda_0$

This translates to a taper efficiency of 0.51 increasing to 0.6. The reason for this relatively low taper efficiency in both the initial and improved design is the $1/r$ decay in amplitude, which for an $F/D = 0.25$ design causes the rays impinging on the edges of the lens to have a significantly lower amplitude compared to the center, even when a short dipole feed is used. The directivity as a function of frequency is plotted in Fig. 5.8(b). Over the complete operating band, an improvement in the directivity can be observed.

5.8 Improved Analysis of Flat Lenses

With knowledge of the ray paths through the lens, one can combine this knowledge with the analytical ADL models, to model the propagation through multiple unit cells. The main idea is to find the unit cells a ray traverses, and at every change to the next unit cell, the geometry and stratification of that new unit cell are used. This can be done by finding the ABCD matrix of a vertical subsection of the unit cell, corresponding to the z-range in which the ray propagated through the unit cell. Fig. 5.9 shows a schematic overview of this method.

The total ABCD matrix can be found as a product of the ABCD matrices for each subsection.

Since in the equivalent transmission line models the bending of the rays cannot be modeled, when computing the S-parameters, the S_{12} of the transmission line model only accounts for the phase shift along z. To also account for the phase shift in the ρ direction and adjusted $S_{12,\text{adj}}$, which takes this into account, is defined as

$$S_{12,\text{adj}} = S_{12} e^{-jk_0 \sin(\theta_i)|\rho_t - \rho_i|} \tag{5.21}$$

where θ_i is the incident angle on the unit cell, ρ_t is the radial distance to the center of the lens from the point where the ray exits the lens P_t, obtained from the ray tracing. ρ_i is the radial distance to the center of the lens at the point where the ray first hits the lens P_i.

Another aspect that must be considered is the spreading of energy. The intensity law of geometric optics [31, p. 115] defines how the intensity of each ray is adjusted and is given by

$$I_1 dS_1 = I_2 dS_2 \,, \tag{5.22}$$

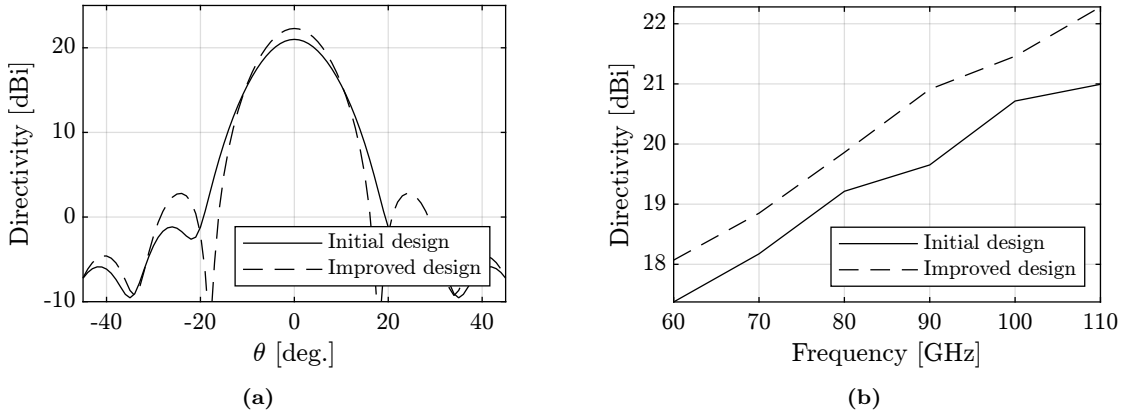

Figure 5.8: (a) Far-field pattern of design without raytracing (initial) and with raytracing (improved). (b) Directivity of design without raytracing (initial) and with raytracing (improved) over frequency.

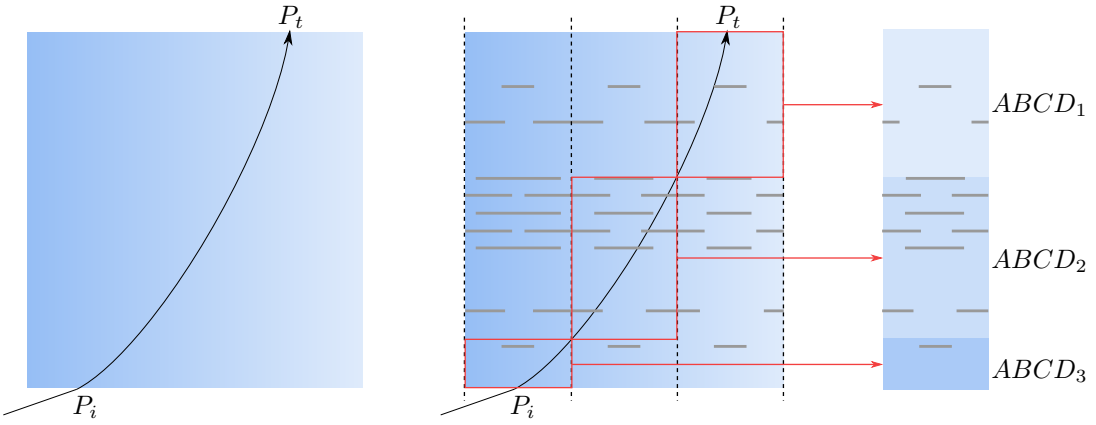

Figure 5.9: Raytracing and finding an equivalent unit cell.

essentially stating that the product of the cross-section dS of a tube, defined by a number of rays, and the intensity of the rays remains constant. If the rays spread, $dS_2 > dS_1$, the intensity of the rays reduces. An illustration of the intensity law of geometric optics is given in Fig. 5.10. Applied to the flat lens, the normal to the surface of the lens is included and can be written as [27]

$$I_1 dS_1 \cos\theta_i = I_2 dS_2 \cos\theta_t \,. \tag{5.23}$$

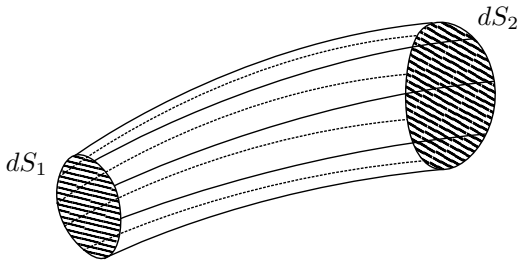

Figure 5.10: Illustration of spreading in the intensity law of geometric optics.

One of the limitations is that in the transmission line model, only homogeneous dielectrics are modeled with horizontal interfaces. By Snell's law, the bending of the rays cannot be modeled, since k_ρ must remain constant, and thus the plane wave has the same angle before and after the lens. The extra information, the horizontal movement of the ray and thus transmit point, and the altered ADL geometry are however included in the model with the proposed hybrid method.

Applying the above-mentioned modifications to the analysis of a lens with a small F/D, the results become more similar to the full-wave simulations. In Fig. 5.12, the far-field patterns are plotted of a lens with $F/D = 0.5$, the same lens for which the patterns were computed without the ray-tracing in Fig. 5.11 (copy of Fig. 4.8). Although the proposed solution is still an approximation compared to the full-wave simulation, a better comparison with CST is obtained. The difference in maximum directivity is less than 0.5 dB.

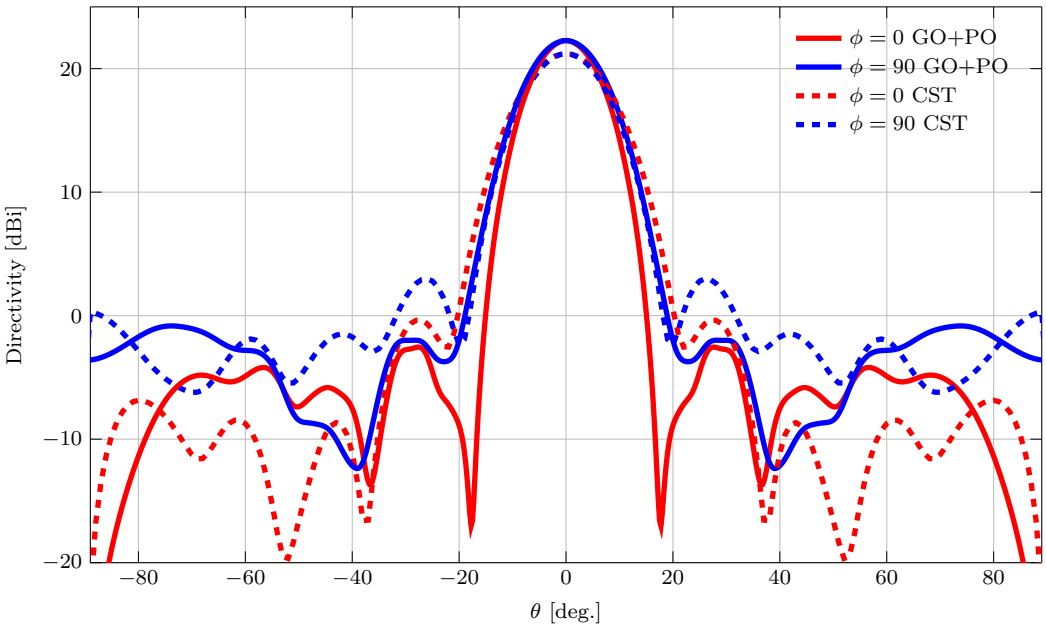

Figure 5.11: Far-field pattern from flat lens with $F/D = 0.25$, computed using CST [23] (dashed) and using the GO/PO analysis without raytracing (solid).

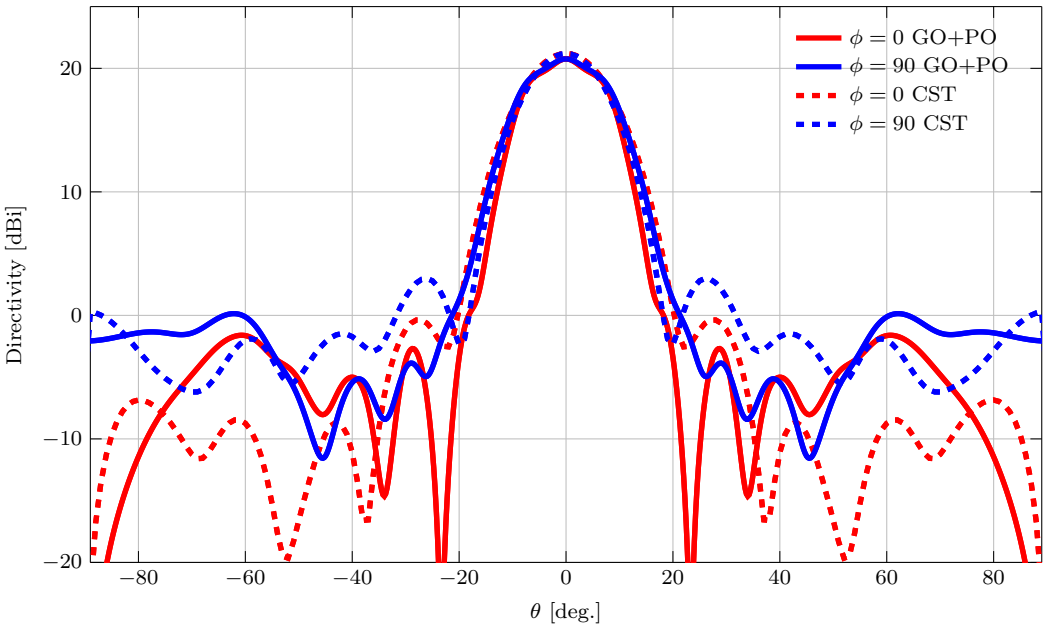

Figure 5.12: Far-field patters of flat lens with $F/D = 0.25$, computed using CST [23] (dashed) and using the GO/PO analysis with raytracing (solid).

Chapter 6

Conclusions and Future Work

6.1 Conclusions

A study on flat lenses based on artificial dielectric layers was presented with the aim of assessing the achievable performance in terms of bandwidth and directivity. First, the optical parameters of the flat lens were related to the maximum phase variation needed across the lens. This range of phase shifts can then be realized with an artificial dielectric unit cell, from which height can be minimized by increasing the effective permittivity of the artificial dielectric. Matching layers were added to realize unit cells with intrinsic low reflection.

A design methodology was presented, showing the feasibility of a lens design combining the low-profile properties of generally narrowband metalenses and Fresnel lenses with the wideband properties of bulky GRIN lenses.

In the lens design example from Section 3.5, a lens with an operating bandwidth of one octave (70-140 GHz) was done. The 11λ diameter lens has a broadside gain of 29.3dB at 140 GHz. Over the entire bandwidth, the total efficiency, including spillover, Ohmic losses, reflection losses, and taper efficiency was $> 63\%$. The total thickness of the lens was $0.85\lambda_{140\text{GHz}}$. The flat property of the lens allows easy integration in antenna systems. If instead a plano-convex dielectric lens, such as the one depicted in Fig. 6.1, had been used with the same diameter, the required thickness would be approximately $3\lambda_{140\text{GHz}}$, 3.5 times thicker.

Note that this 3.5 times reduction in thickness must be viewed considering the total lens system, including the feed. Since this particular lens has a diameter of 11λ, and $F/D = 1$, the total length occupied by the system is 11.85λ compared to 14λ, a reduction of 15%. The advantages

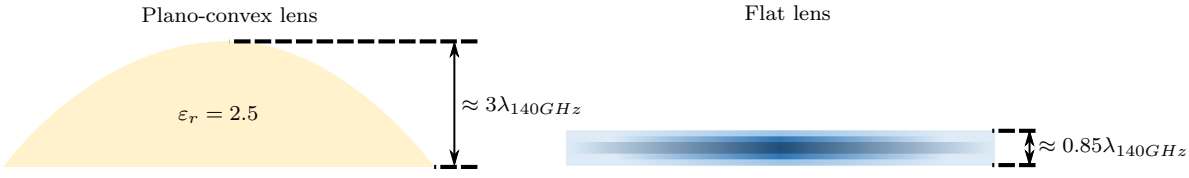

Figure 6.1: Thickness comparison between a plano-convex lens and the example flat lens design.

in thickness reduction could pay off more when the feed is placed closer to the lens, or directly attached to the lens. Besides the design, a GO/PO method was used to model the lens and assess the performance. For $F/D = 1$, a design was presented and used to compare the performance of the analytical model compared to full-wave simulations of the lens. For that particular F/D ratio, the analytical model agrees well with the full-wave simulations in terms of main beam shape and directivity.

For smaller F/D and larger scan angles, the effect of rays propagating through multiple unit cells becomes visible, giving a decreased accuracy of the GO/PO model. To mitigate this, ray propagation in non-homogeneous media was studied. Using the information gained from running a ray-tracing program on a lens design, one can find the unit cells that each ray traverses and construct equivalent unit cells, that combine relevant portions of different unit cells. This resulted in a more accurate result from the GO/PO method, for small F/D and potentially also for large scan angles.

Apart from improving the lens analysis, a ray-tracing program can be used to adjust the lens design based on homogeneous dielectrics, and consequently improve the performance of the lens realized in ADLs.

6.2 Future Work

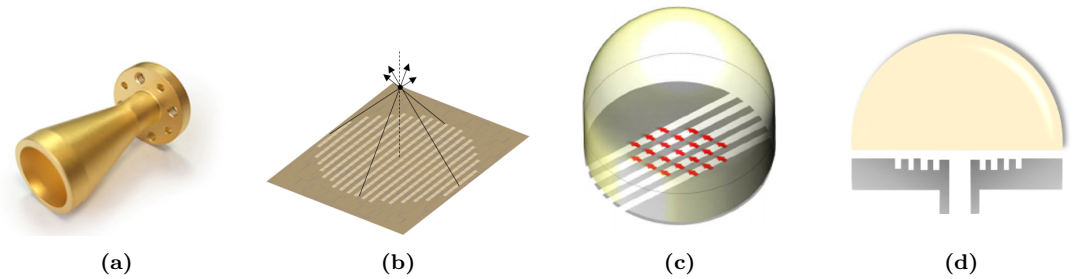

Figure 6.2: Possible lens feeds: (a) Horn antenna, (b) Near-field focused connected array (c) Connected-array-fed hyper-hemispherical lens (d) Hemispherical lens fed with corrugated waveguide.

Co-design lens with feed: A well-matched antenna with stable patterns over the operational bandwidth is required to illuminate the flat lens. Until now, a feed with frequency-stable patterns was assumed to be available. The co-design of such a feed is out of the scope of this thesis. However, several options for feeds have been considered.

The first option is to use a horn antenna, like the one in Fig. 6.2(a). At microwave frequencies, wideband horn antenna designs exist [32], [33]. Despite not being readily available for mmWave, one could design a horn antenna with the required properties.

Another option would be to use a near-field focused connected array [34]. In Fig. 6.2(b) a schematic of such an antenna is displayed. It has stable patterns over a 1:2 frequency band. A feeding network is however needed, which introduces losses to the system. Similarly, [35] describes a hyper-hemispherical lens made of silicon fed by a connected array, as depicted in Fig. 6.2(c). The connected array also requires a feeding network and thus introduces losses. Furthermore, the silicon lens causes reflection losses. This lens does however provide stable patterns over a 1:3 bandwidth.

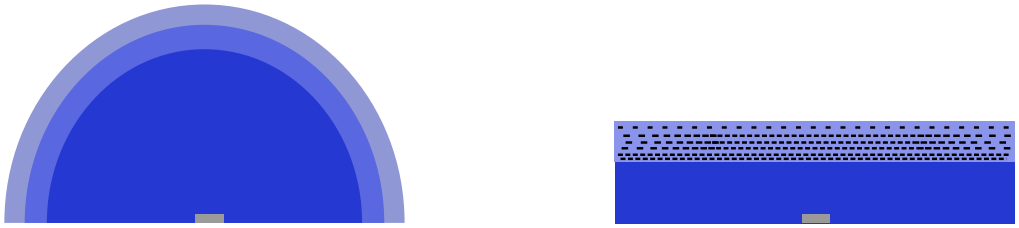

(a) (b)

Figure 6.3: (a) Silicon lens with multi-layer anti-reflection coating. (b) Flat lens combined with a silicon substrate.

A simpler option would be a hemispherical lens fed with a corrugated waveguide [36], like the antenna shown in Fig. 6.2(d). The hemispherical lens is made from a low-permittivity material, so reflection losses are low. Since no feeding network is required, the overall losses of this feed option are low. This structure has stable patterns over a 50% bandwidth.

More complex lenses: Using this design method proposed here, any phase distribution can be created after the lens. This would allow achieving more general types of radiation patterns, such as squinted beams from broadside, shaped beams, or near-field focused beams. For example, the lens designs presented in the thesis were optimized for an on-axis feed, but similarly an optimization of the performance could be done for off-axis feed placements.

Investigate further integration: Further integration could be investigated, for example, smaller F/D, or a lens with the feed directly attached to the lens. This could be especially advantageous for high-frequency (terahertz) antennas, which typically resort to silicon lenses integrated with the electronic chips, such as the lens depicted in Fig. 6.3(a). One limitation of elliptical or hyper-hemispherical lenses is that matching layers are required on the top surface of the lens to avoid strong reflections at the dielectric-air interface. The practical realization of the matching layers is problematic, because a single-layer anti-reflection coating is narrowband, while wideband anti-reflection coatings based on multiple layers of machined grooves are extremely difficult to realize on curved surfaces. These problems could be avoided by replacing the standard curved lenses with flat lenses based on artificial dielectrics. A schematic drawing of such a lens is shown in Fig. 6.3(b).

Experimental validation: There are several things to consider if one is to manufacture a flat lens based on artificial dielectric layers. In the example design, permittivities lower than the host material must be realized.

One way to do this is by making sub-wavelength perforations in the material. In principle, any permittivity can be created. This is however very difficult to manufacture, especially because one does not always require holes that go through all layers or need the same diameter in all layers. Another method to achieve these low permittivity sections would be to use a dielectric with an actual lower permittivity for the outer matching layer and make sub-wavelength cuts in the periphery of the lens, to achieve a lower equivalent permittivity. Both methods have been simulated and give a comparable directivity as lenses simulated with homogeneous dielectrics.

Another way to deal with this would be to increase the permittivity at the edges of the lens to be equal to the permittivity of the host material. This eases manufacturing, but comes at the

cost of requiring a higher phase shift in the center of the lens and thus possibly a thicker lens.

For complex designs with a large number of metal layers, the cost of manufacturing could be reduced by making a symmetric design of the top and bottom half of the lens, such that only half the number of metal layers is required. To reduce the cost further, one could make a design in which the inter-metallayer distance is constant. The different components of the lens can be manufactured next to each other on a cheap single-layer PCB and assembled into a lens by stacking the different components.

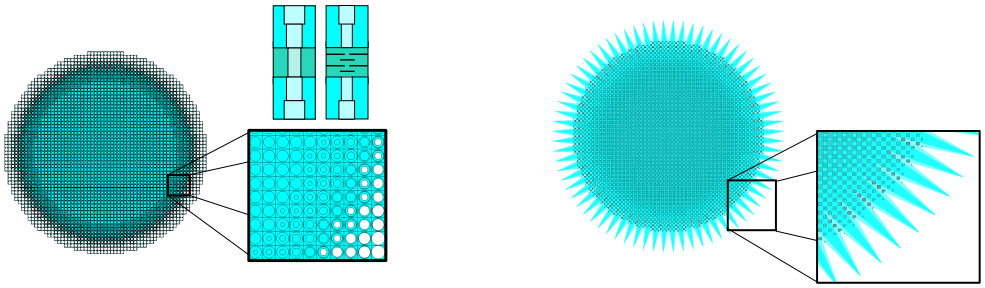

(a) **(b)**

Figure 6.4: Two different methods as a means to achieve lower equivalent permittivity values than the dielectric: (a) perforations through (part) of the unit cells, and (b) sub-wavelength cuts in the periphery of the lens.

Bibliography

[1] W. Hong, Z. H. Jiang, C. Yu, *et al.*, "Multibeam antenna technologies for 5g wireless communications," *IEEE Transactions on Antennas and Propagation*, vol. 65, no. 12, pp. 6231–6249, 2017. DOI: 10.1109/TAP.2017.2712819.

[2] A. Jouade, M. Himdi, and O. Lafond, "Fresnel lens at millimeter-wave: Enhancement of efficiency and radiation frequency bandwidth," *IEEE Transactions on Antennas and Propagation*, vol. 65, no. 11, pp. 5776–5786, 2017. DOI: 10.1109/TAP.2017.2755120.

[3] G. Liu, M. R. Dehghani Kodnoeih, K. T. Pham, E. M. Cruz, D. González-Ovejero, and R. Sauleau, "A millimeter-wave multibeam transparent transmitarray antenna at ka-band," *IEEE Antennas and Wireless Propagation Letters*, vol. 18, no. 4, pp. 631–635, 2019. DOI: 10.1109/LAWP.2019.2899925.

[4] M. Jiang, Z. N. Chen, Y. Zhang, W. Hong, and X. Xuan, "Metamaterial-based thin planar lens antenna for spatial beamforming and multibeam massive mimo," *IEEE Transactions on Antennas and Propagation*, vol. 65, no. 2, pp. 464–472, 2017. DOI: 10.1109/TAP.2016.2631589.

[5] S. Silver, Ed., *Microwave antenna theory and design*, ser. Electromagnetics and Radar. Stevenage, England: Institution of Engineering and Technology, Jun. 1984.

[6] A. Paraskevopoulos, F. Maggiorelli, M. Albani, and S. Maci, "Radial grin lenses based on the solution of a regularized ray congruence equation," *IEEE Transactions on Antennas and Propagation*, vol. 70, no. 2, pp. 888–899, 2022. DOI: 10.1109/TAP.2021.3111315.

[7] F. Maggiorelli, A. Paraskevopoulos, J. C. Vardaxoglou, M. Albani, and S. Maci, "Profile inversion and closed form formulation of compact grin lenses," *IEEE Open Journal of Antennas and Propagation*, vol. 2, pp. 315–325, 2021. DOI: 10.1109/OJAP.2021.3059468.

[8] N. C. Garcia and J. D. Chisum, "High-efficiency, wideband grin lenses with intrinsically matched unit cells," *IEEE Transactions on Antennas and Propagation*, vol. 68, no. 8, pp. 5965–5977, 2020. DOI: 10.1109/TAP.2020.2990289.

[9] S. S. D. Jones and J. Brown, "Metallic delay lenses," *Nature*, vol. 163, no. 4139, pp. 324–325, Feb. 1949. DOI: 10.1038/163324a0. [Online]. Available: https://doi.org/10.1038/163324a0.

[10] M. Li and N. Behdad, "Wideband true-time-delay microwave lenses based on metallo-dielectric and all-dielectric lowpass frequency selective surfaces," *IEEE Transactions on Antennas and Propagation*, vol. 61, no. 8, pp. 4109–4119, 2013. DOI: 10.1109/TAP.2013.2263784.

[11] D. Cavallo, W. H. Syed, and A. Neto, "Closed-form analysis of artificial dielectric layers—part I: Properties of a single layer under plane-wave incidence," *IEEE Transactions on Antennas and Propagation*, vol. 62, no. 12, pp. 6256–6264, Dec. 2014.

[12] D. Cavallo, W.H. Syed and A. Neto, "Closed-form analysis of artificial dielectric layers—part II: Extension to multiple layers and arbitrary illumination," *IEEE Transactions on Antennas and Propagation*, vol. 62, no. 12, pp. 6265–6273, Dec. 2014.

[13] D. Cavallo and C. Felita, "Analytical formulas for artificial dielectrics with nonaligned layers," *IEEE Transactions on Antennas and Propagation*, vol. 65, no. 10, pp. 5303–5311, Oct. 2017.

[14] D. Cavallo, "Dissipation losses in artificial dielectric layers," *IEEE Transactions on Antennas and Propagation*, vol. 66, no. 12, pp. 7460–7465, 2018. DOI: 10.1109/TAP.2018.2869241.

[15] D. Cavallo and R. M. van Schelven, "Closed-form analysis of artificial dielectric layers with non-periodic characteristics," in *2019 13th European Conference on Antennas and Propagation (EuCAP)*, Mar. 2019, pp. 1–5.

[16] R. E. Collin, *Foundations for Microwave Engineering*, en, 2nd ed., ser. IEEE Press Series on Electromagnetic Wave Theory. Nashville, TN: John Wiley & Sons, Dec. 2001.

[17] D. M. Pozar, *Microwave Engineering*, en, 4th ed. Chichester, England: John Wiley & Sons, Nov. 2011.

[18] D. Frickey, "Conversions between s, z, y, h, abcd, and t parameters which are valid for complex source and load impedances," *IEEE Transactions on Microwave Theory and Techniques*, vol. 42, no. 2, pp. 205–211, 1994. DOI: 10.1109/22.275248.

[19] W. H. Syed, D. Cavallo, H. Thippur Shivamurthy, and A. Neto, "Wideband, wide-scan planar array of connected slots loaded with artificial dielectric superstrates," *IEEE Transactions on Antennas and Propagation*, vol. 64, no. 2, pp. 543–553, Feb. 2016.

[20] D. Cohen and R. Shavit, "Bi-anisotropic metamaterials effective constitutive parameters extraction using oblique incidence s-parameters method," *IEEE Transactions on Antennas and Propagation*, vol. 63, no. 5, pp. 2071–2078, 2015. DOI: 10.1109/TAP.2015.2405078.

[21] W. Syed, "On the control of surface waves in integrated antennas: Analysis and design exploiting artificial dielectric layers," Ph.D. dissertation, Delft University Of Technology, 2015.

[22] *Ro4350b™ laminates*. [Online]. Available: https://rogerscorp.com/advanced-electronics-solutions//ro4000-series-laminates/ro4350b-laminates.

[23] CST, a Dassault Systemes company, *Cst studio suite 2018*, version 2018.01, Nov. 17, 2017. [Online]. Available: https://cst.com/.

[24] T. A. Milligan, *Modern Antenna Design*, en, 2nd ed., ser. Wiley - IEEE. Nashville, TN: John Wiley & Sons, Jun. 2005.

[25] "Integrated circuits – measurement of electromagnetic emissions – part 1-1: General conditions and definitions – near-field scan data exchange format," International Electrotechnical Commission, Tech. Rep. IEC TR 61967-1-1, Aug. 2015. [Online]. Available: https://webstore.iec.ch/preview/info_iec61967-1-1%7Bed2.0%7Den.pdf.

[26] J. Clerk Maxwell, "Solutions of problems," *Cambridge and Dublin Mathematical Journal*, vol. 8, pp. 188–189, Feb. 1854.

[27] F. Maggiorelli, A. Paraskevopoulos, R. Giusto, M. Albani, and S. Maci, "Ray-tracing in dielectric inhomogeneous metalenses," in *2021 15th European Conference on Antennas and Propagation (EuCAP)*, 2021, pp. 1–5. DOI: 10.23919/EuCAP51087.2021.9411505.

[28] S. Zhang, R. K. Arya, W. G. Whittow, D. Cadman, R. Mittra, and J. C. Vardaxoglou, "Ultra-wideband flat metamaterial grin lenses assisted with additive manufacturing technique," *IEEE Transactions on Antennas and Propagation*, vol. 69, no. 7, pp. 3788–3799, 2021. DOI: 10.1109/TAP.2020.3044586.

[29] M. Sluijter, D. K. G. de Boer, and J. J. M. Braat, "General polarized ray-tracing method for inhomogeneous uniaxially anisotropic media," en, *J. Opt. Soc. Am. A Opt. Image Sci. Vis.*, vol. 25, no. 6, pp. 1260–1273, Jun. 2008.

[30] C. G. Parazzoli, B. E. C. Koltenbah, R. B. Greegor, T. A. Lam, and M. H. Tanielian, "Eikonal equation for a general anisotropic or chiral medium: Application to a negative-graded index-of-refraction lens with an anisotropic material," *J. Opt. Soc. Am. B*, vol. 23, no. 3, pp. 439–450, Mar. 2006. DOI: 10.1364/JOSAB.23.000439. [Online]. Available: http://opg.optica.org/josab/abstract.cfm?URI=josab-23-3-439.

[31] M. Born and E. Wolf, *Principles of optics: electromagnetic theory of propagation, interference and diffraction of light; 2nd ed.* Oxford: Pergamon, 1964.

[32] M. Abbas-Azimi, F. Mazlumi, and F. Behnia, "Design of broadband constant-beamwidth conical corrugated-horn antennas [antenna designer's notebook]," *IEEE Antennas and Propagation Magazine*, vol. 51, no. 5, pp. 109–114, 2009. DOI: 10.1109/MAP.2009.5432055.

[33] B. Lee, A. Gonzalez, K. Kaneko, R. Sakai, and J.-W. Lee, "Design and characterization of 275-500 ghz corrugated horns and optics for a wideband radio astronomy receiver," in *2020 14th European Conference on Antennas and Propagation (EuCAP)*, 2020, pp. 1–4. DOI: 10.23919/EuCAP48036.2020.9135944.

[34] A. Pascual Laguna, D. Cavallo, J. J. A. Baselmans, and N. Llombart, "Focused connected array antenna as a broadband beam-steering feed for quasi-optical system," *IEEE Transactions on Antennas and Propagation*, vol. 70, no. 7, pp. 5995–6000, 2022. DOI: 10.1109/TAP.2022.3142291.

[35] O. Yurduseven, D. Cavallo, and A. Neto, "Wideband dielectric lens antenna with stable radiation patterns fed by coherent array of connected leaky slots," *IEEE Transactions on Antennas and Propagation*, vol. 62, no. 4, pp. 1895–1902, 2014. DOI: 10.1109/TAP.2014.2298875.

[36] M. Alonso-delPino, N. van Rooijen, S. Bosma, and N. Llombart, "A wideband corrugated leaky-wave feed with low cross-pol for high efficiency lens illumination," in *15th European Conference on Antennas and Propagation (EuCAP)*, Düsseldorf, Germany, Mar. 2021.

Appendix A

Chebyshev Multi-Section Transformer: General Expression for Arbitrary Order n

The scope of this appendix is to describe the steps to derive the characteristic impedances Z_n in a N-section Chebyshev transformer (see figure below). The procedure is described for a few specific values of N in [17], while here a general expression is derived that is valid for arbitrary N.

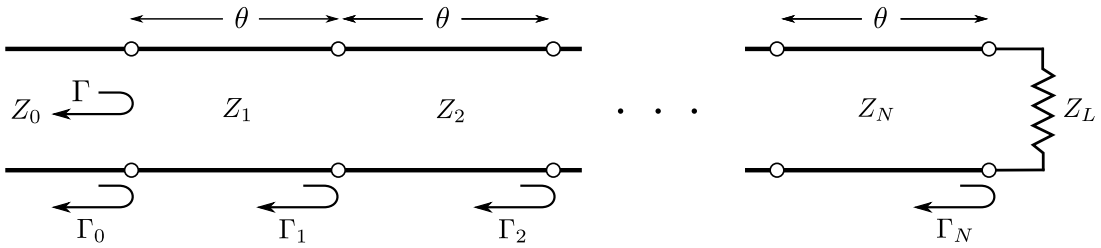

Figure A.1: Reflections on a transmission line with multiple sections. [17]

The nth-order Chebyshev polynomial is a polynomial of degree n, denoted by $T_n(x)$. The first two Chebyshev polynomials are

$$T_0(x) = 1 \tag{A.1}$$

$$T_1(x) = x \tag{A.2}$$

and for all higher order, one can apply iteratively

$$T_n(x) = 2xT_{n-1}(x) - T_{n-2}(x)\,. \tag{A.3}$$

The Chebyshev polynomial can be expressed explicitly as a sum

$$T_n(x) = \frac{n}{2}\sum_{k=0}^{\lfloor \frac{n}{2} \rfloor}(-1)^k \frac{(n-k-1)!}{k!(n-2k)!}(2x)^{n-2k} \quad \text{for } n > 0\,. \tag{A.4}$$

The reflection coefficient of a multi-section transformer with N sections of length l can be written, according to the theory of small reflections [17, p. 252] as

$$\Gamma(\theta) = \begin{cases} 2e^{-jN\theta} \displaystyle\sum_{n=0}^{(N-1)/2} \Gamma_n \cos((N-2n)\theta) & N \text{ odd} \\ 2e^{-jN\theta} \left(\displaystyle\sum_{n=0}^{N/2-1} \Gamma_n \cos((N-2n)\theta) + \frac{1}{2}\Gamma_{N/2} \right) & N \text{ even} \end{cases} \tag{A.5}$$

where $\theta = \beta l$, β is the phase constant of the transmission line sections, l is the section length, and Γ_n are the partial reflection coefficients:

$$\Gamma_n = \frac{Z_{n+1} - Z_n}{Z_{n+1} + Z_n} \tag{A.6}$$

with $Z_{N=1} = Z_L$. To synthesize a multi-section Chebyshev equal-ripple passband, we equate the reflection coefficient to the Chebyshev polynomial:

$$\Gamma(\theta) = Ae^{-jN\theta} T_N(\sec\theta_m \cos\theta) \tag{A.7}$$

where $\sec\theta_m$ is a parameter depending on the transformation ratio Z_L/Z_0 and the pass band ripple Γ_m and can be approximated as

$$\sec\theta_m \approx \cosh\left[\frac{1}{N} \cosh^{-1}\left(\left| \frac{\ln(Z_L/Z_0)}{2\Gamma_m} \right| \right) \right]. \tag{A.8}$$

The constant A can be found by imposing the boundary condition (letting $\theta = 0$, corresponding to zero frequency) as

$$A = \frac{Z_L - Z_0}{Z_L + Z_0} \frac{\Gamma_m}{\left| \dfrac{Z_L - Z_0}{Z_L + Z_0} \right|}. \tag{A.9}$$

To find the values of the impedances Z_n in the multi-section transformer one can write

N odd
$$2e^{-jN\theta} \sum_{n=0}^{(N-1)/2} \Gamma_n \cos((N-2n)\theta) = Ae^{-jN\theta} T_N(\sec\theta_m \cos\theta) \tag{A.10}$$

N even
$$2e^{-jN\theta} \left(\sum_{n=0}^{N/2-1} \Gamma_n \cos((N-2n)\theta) + \frac{1}{2}\Gamma_{N/2} \right) = Ae^{-jN\theta} T_N(\sec\theta_m \cos\theta) \tag{A.11}$$

Case 1: N odd

$$2 \sum_{n=0}^{(N-1)/2} \Gamma_n \cos((N-2n)\theta) = AT_N(\sec\theta_m \cos\theta) \tag{A.12}$$

From the explicit expression of the polynomial

$$T_N(\sec\theta_m \cos\theta) = \frac{N}{2} \sum_{n=0}^{\lfloor \frac{N}{2} \rfloor} (-1)^n \frac{(N-n-1)!}{n!(N-2n)!} (2\sec\theta_m)^{N-2n} \cos^{N-2n}(\theta) \tag{A.13}$$

Expanding the power of a cosine as follows:

$$\cos^l\theta = \frac{1}{2^l}\sum_{p=0}^{l}\binom{l}{p}\cos((2p-l)\theta) \tag{A.14}$$

$$T_N(\sec\theta_m\cos\theta) \tag{A.15}$$

$$= \frac{N}{2}\sum_{n=0}^{\lfloor\frac{N}{2}\rfloor}(-1)^n\frac{(N-n-1)!}{n!(N-2n)!}(2\sec\theta_m)^{N-2n}\frac{1}{2^{N-2n}}\sum_{p=0}^{N-2n}\binom{N-2n}{p}\cos((2p-N+2n)\theta) \tag{A.16}$$

$$= \frac{N}{2}\sum_{n=0}^{\lfloor\frac{N}{2}\rfloor}(-1)^n\frac{(N-n-1)!}{n!(N-2n)!}(2\sec\theta_m)^{N-2n}\frac{1}{2^{N-2n}}\sum_{p=0}^{N-2n}\frac{(N-2n)!}{p!(N-2n-p)!}\cos((2p-N+2n)\theta) \tag{A.17}$$

$$= \frac{N}{2}\sum_{n=0}^{\lfloor\frac{N}{2}\rfloor}(-1)^n\frac{(N-n-1)!}{n!}(\sec\theta_m)^{N-2n}\sum_{p=0}^{N-2n}\frac{1}{p!(N-2n-p)!}\cos((2p-N+2n)\theta) \tag{A.18}$$

$$= \frac{N}{2}\sum_{n=0}^{\lfloor\frac{N}{2}\rfloor}\sum_{p=0}^{N-2n}a(n,p,N)(sec\theta_m)^{N-2n}\cos((2p-N+2n)\theta) \tag{A.19}$$

where

$$a(n,p,N) \triangleq (-1)^n\frac{(N-n-1)!}{n!p!(N-2n-p)!} \tag{A.20}$$

Substituting Eq. (A.19) in Eq. (A.12) one obtains

$$2\sum_{n=0}^{(N-1)/2}\Gamma_n\cos((N-2n)\theta) = A\frac{N}{2}\sum_{n'=0}^{\lfloor\frac{N}{2}\rfloor}\sum_{p=0}^{N-2n'}a(n',p,N)(\sec\theta_m)^{N-2n'}\cos((2p-N+2n')\theta)\,. \tag{A.21}$$

One can note that each value of n in the left hand side (LHS) gives rise to one term in the form of $\cos(l_{\mathrm{LHS}}\theta)$ where l_{LHS} is an odd integer $[1,3,...N]$. Similarly in the right hand side (RHS) a $\cos(\pm l_{\mathrm{RHS}}\theta)$ term appears for each combination of the indexes n' and p. The following scheme can be observed for the indexes:

LHS		Example $N=5$	
n	$l_{LHS}=N-2n$	n	l_{LHS}
0	N	0	5
1	$N-2$	1	3
...	...	2	1
$\lfloor\frac{N}{2}\rfloor$	1		

RHS

n'	p	$l_{RHS} = 2p - N + 2n'$	$n' + p$
0	0	$-N$	0
	...	$-N+2$	...
	...	...	...
	N	N	N
1	0	$-N+2$	1
	1	$-N+4$	2
	...	...	...
	$N-2$	$N-2$	$N-1$
...	...	...	...
$\left\lfloor \frac{N}{2} \right\rfloor$	0	$-N+2\left\lfloor \frac{N}{2} \right\rfloor$	$\left\lfloor \frac{N}{2} \right\rfloor$
	...	...	...
	$N-2\left\lfloor \frac{N}{2} \right\rfloor$	$N-2\left\lfloor \frac{N}{2} \right\rfloor$	$N-\left\lfloor \frac{N}{2} \right\rfloor$

Example $N = 5$

n'	p	$\lvert l_{RHS} \rvert$	$n' + p$
0	0	5	0
	1	3	1
	2	1	2
	3	1	3
	4	3	4
	5	5	5
1	0	3	1
	1	1	2
	2	1	3
	3	3	4
2	0	1	2
	1	1	3

From comparing the indexes on the LHS and RHS one can equate the coefficient of the terms $\cos(l_{LHS}\theta)$ and $\cos(|l_{RHS}|\theta)$ as follows

$$\Gamma_n = A\frac{N}{4}\sum_{n'=0}^{\lfloor \frac{N}{2} \rfloor}\sum_{p=0}^{N-2n'} a(n',p,N)(\sec\theta_m)^{N-2n'}U(n'+p \in [n, N-n]) \tag{A.22}$$

where

$$U(n'+p \in [n, N-n]) = \begin{cases} 1 & \text{for } n'+p = n \text{ or } n'+p = N-n \\ 0 & \text{otherwise} \end{cases} \tag{A.23}$$

and

$$a(n',p,N) = (-1)^{n'}\frac{(N-n'-1)!}{n'!p!(N-2n'-p)!} \tag{A.24}$$

Case 2: N even

$$2\left(\sum_{n=0}^{N/2-1}\Gamma_n\cos((N-2n)\theta) + \frac{1}{2}\Gamma_{N/2}\right) = AT_N(\sec\theta_m\cos\theta) \tag{A.25}$$

$$2\left(\sum_{n=0}^{N/2-1}\Gamma_n\cos((N-2n)\theta) + \frac{1}{2}\Gamma_{N/2}\right) = A\frac{N}{2}\sum_{n'=0}^{\lfloor \frac{N}{2} \rfloor}\sum_{p=0}^{N-2n'} a(n',p,N)(\sec\theta_m)^{N-2n'}\cos((2p-N+2n')\theta) \tag{A.26}$$

Similar to the odd case, the $\cos(l_{LHS}\theta)$ and $\cos(|l_{RHS}|\theta)$ terms appear on the LHS and RHS according to the following pattern:

From comparing the indexes on the LHS and RHS one can equate the coefficient of the terms $\cos(l_{LHS}\theta)$ and $\cos(|l_{RHS}|\theta)$ as follows

$$\Gamma_n = A\frac{N}{4}\sum_{n'=0}^{\lfloor \frac{N}{2} \rfloor}\sum_{p=0}^{N-2n'} a(n',p,N)(\sec\theta_m)^{N-2n'}U(n'+p \in [n, N-n]) \text{ for } n < \frac{N}{2} \tag{A.27}$$

LHS

n	$l_{LHS} = N - 2n$
0	N
1	$N-2$
...	...
$N/2-1$	2
$N/2$	0

Example $N = 6$

n	l_{LHS}
0	6
1	4
2	2
3	0

RHS

n'	p	$l_{RHS} = 2p - N + 2n'$	$n' + p$
0	0	$-N$	0
	...	$-N+2$	...
	...	...	...
	N	N	N
1	0	$-N+2$	1
	1	$-N+4$	2
	...	...	...
	$N-2$	$N-2$	$N-1$
...	...	...	...
$N/2$	0	0	$N/2$

Example $N = 6$

n'	p	$\lvert l_{RHS}\rvert$	$n' + p$
0	0	6	0
	1	4	1
	2	2	2
	3	0	3
	4	2	4
	5	4	5
	6	6	6
1	0	4	1
	1	2	2
	2	0	3
	3	2	4
	4	4	5
2	0	2	2
	1	0	3
	2	2	4
3	0	0	3

$$\Gamma_{\frac{N}{2}} = A\frac{N}{2}\sum_{n'=0}^{\lfloor \frac{N}{2} \rfloor}\sum_{p=0}^{N-2n'} a(n', p, N)(\sec\theta_m)^{N-2n'} U(n' + p \in [n, N-n]) \tag{A.28}$$

where

$$U(n' + p \in [n, N-n]) = \begin{cases} 1 & \text{for } n' + p = n \text{ or } n' + p = N - n \\ 0 & \text{otherwise} \end{cases} \tag{A.29}$$

and

$$a(n', p, N) = (-1)^{n'} \frac{(N - n' - 1)!}{n'!p!(N - 2n' - p)!}. \tag{A.30}$$

Section impedances

Finally, from Γ_n the impedance of the sections can be found as

$$Z_{n+1} \approx e^{(\ln(Z_n) + 2\Gamma_n)}. \tag{A.31}$$

Appendix B

Far-field from Planar Current Distribution

This appendix describes how to compute the far-field radiated by a planar current in the x-y plane at height z_0.

Consider an electric current defined on a planar surface

$$j(x,y)\delta(z-z_0)\,. \tag{B.1}$$

The e-field resulting from this current in free space is computed as the convolution of the current with dyadic Green's function for free space.

$$\boldsymbol{e}(x,y,z) = \iiint_V \boldsymbol{j}(x',y')\delta(z'-z_0)\boldsymbol{g}(x-x',y-y',z-z')dx'dy'dz' \tag{B.2}$$

The integral in z' is closed by evaluating in $z'=z_0$:

$$\boldsymbol{e}(x,y,z) = \iint_S \boldsymbol{j}(x',y')\boldsymbol{g}(x-x',y-y',z-z_0)dx'dy'\,. \tag{B.3}$$

Writing the Green's function as the inverse Fourier transform of the spectral Green's function $\boldsymbol{G}$ yields

$$\boldsymbol{g}(x-x',y-y',z-z_0) = \frac{1}{4\pi^2}\int_{-\infty}^{\infty}\int_{-\infty}^{\infty}\boldsymbol{G}(k_x,k_y,z-z_0)e^{-jk_x(x-x')}e^{-jk_y(y-y')}dk_xdk_y\,. \tag{B.4}$$

One can substitute this back in Eq. (B.3):

$$\boldsymbol{e}(x,y,z) = \iint_S \boldsymbol{j}(x',y')\frac{1}{4\pi^2}\int_{-\infty}^{\infty}\int_{-\infty}^{\infty}\boldsymbol{G}(k_x,k_y,z-z_0)e^{-jk_x(x-x')}e^{-jk_y(y-y')}dk_xdk_ydx'dy'\,. \tag{B.5}$$

Regrouping the terms depending on x' and y', we can write

$$\boldsymbol{e}(x,y,z) = \frac{1}{4\pi^2}\int_{-\infty}^{\infty}\int_{-\infty}^{\infty}\boldsymbol{G}(k_x,k_y,z-z_0)\left(\iint_S \boldsymbol{j}(x',y')e^{jk_xx'}e^{jk_yy'}dx'dy'\right)e^{-jk_xx}e^{-jk_yy}dk_xdk_y \tag{B.6}$$

We now recognize that the term between parentheses is the two-dimensional spatial Fourier transform $\boldsymbol{J}$ of the current distribution:

$$\boldsymbol{e}(x,y,z) = \frac{1}{4\pi^2}\int_{-\infty}^{\infty}\int_{-\infty}^{\infty}\boldsymbol{G}(k_x,k_y,z-z_0)\boldsymbol{J}(k_x,k_y)e^{-jk_x x}e^{-jk_y y}dk_x dk_y \tag{B.7}$$

Using asymptotic evaluation of the integral in the far-field based on the stationary phase point contribution, one can approximate the far-field as

$$\boldsymbol{E}_{far}(r,\theta,\phi) \approx jk_z\widetilde{\boldsymbol{G}}^{\boldsymbol{ej}}(k_x,k_y,z,z_0)\boldsymbol{J}(k_x,k_y)e^{jk_z|z-z_0|}\frac{e^{-jkr}}{2\pi r}\,, \tag{B.8}$$

where the spectral Green's function for free space $\widetilde{\boldsymbol{G}}^{\boldsymbol{ej}}(k_x,k_y,z,z_0)$ to relate the E-field to the Fourier transform of an electric current $\boldsymbol{J}$ is given by

$$\widetilde{\boldsymbol{G}}^{\boldsymbol{ej}}(k_x,k_y,z,z_0) = \frac{-\zeta}{2kk_z}\begin{bmatrix} k^2-k_x^2 & -k_xk_y & -k_x(\pm k_z) \\ -k_yk_x & k^2-k_y^2 & -k_y(\pm k_z) \\ -(\pm k_z)k_x & -(\pm k_z)k_y & -2j\delta(z-z_0)+(k^2-k_z^2) \end{bmatrix}. \tag{B.9}$$

The sign for k_z is chosen as:

$$\begin{aligned} z-z_0>0 &\Rightarrow +k_z \\ z-z_0<0 &\Rightarrow -k_z\,. \end{aligned} \tag{B.10}$$

B.1 Fourier Transform of Truncated Gaussian Distribution

When considering a Gaussian current distribution for the lens feed, it can be convenient to find an expression of the Fourier transform to find the primary pattern illuminating the lens, with the procedure described in the previous section. The one-dimensional Fourier transform can be written as

$$\int_{-\frac{A}{2}}^{\frac{A}{2}} e^{-\frac{x^2}{w_0^2}}e^{jk_x x}dx\,. \tag{B.11}$$

Splitting the regions above and below zero yields

$$\int_{-\frac{A}{2}}^{\frac{A}{2}} e^{-\frac{x^2}{w_0^2}}e^{jk_x x}dx = \int_{-\frac{A}{2}}^{0} e^{-\frac{x^2}{w_0^2}}e^{jk_x x}dx + \int_{0}^{\frac{A}{2}} e^{-\frac{x^2}{w_0^2}}e^{jk_x x}dx\,. \tag{B.12}$$

Substitute $x' = -x$ in the first integral:

$$\int_{\frac{A}{2}}^{0} e^{-\frac{x'^2}{w_0^2}}e^{jk_x x'}dx' + \int_{0}^{\frac{A}{2}} e^{-\frac{x^2}{w_0^2}}e^{jk_x x}dx = \int_{0}^{\frac{A}{2}} e^{-\frac{x^2}{w_0^2}}e^{-jk_x x}dx + \int_{0}^{\frac{A}{2}} e^{-\frac{x^2}{w_0^2}}e^{jk_x x}dx\,. \tag{B.13}$$

Taking the integrals together results in

$$\int_{0}^{\frac{A}{2}} e^{-\frac{x^2}{w_0^2}}(e^{jk_x x}e^{-jk_x x})dx = \int_{0}^{\frac{A}{2}} e^{-\frac{x^2}{w_0^2}}2\cos(k_x x)dx \tag{B.14}$$

which can be written as

$$\int_{0}^{\frac{A}{2}} e^{-\frac{x^2}{w_0^2}}2\cos(k_x x)dx = \frac{w_0}{2}\sqrt{\pi}e^{-\frac{w_0^2k_x^2}{4}}\left[\operatorname{erf}\left(\frac{jk_xw_0^2+A}{2w_0}\right)-\operatorname{erf}\left(\frac{jk_xw_0^2-A}{2w_0}\right)\right]. \tag{B.15}$$

In this expression, the erf is the complex error function, which can be written as an infinite sum

$$\operatorname{erf}(z) = \frac{2}{\sqrt{\pi}}\sum_{n=0}^{\infty}\frac{(-1)^n x^{2n+1}}{n!(2n+1)}\,. \tag{B.16}$$

Appendix C

Derivation of the Eikonal Equation

This procedure is based on the formalism presented in [31].

C.1 The Eikonal Equation From the Maxwell Equations

Time-harmonic electromagnetic fields can be written in terms of the corresponding phasors as

$$\boldsymbol{e}(\boldsymbol{r},t) = \Re\{\boldsymbol{E}(\boldsymbol{r})e^{j\omega t}\}, \boldsymbol{h}(\boldsymbol{r},t) = \Re\{\boldsymbol{H}(\boldsymbol{r})e^{j\omega t}\}\,. \tag{C.1}$$

In the absence of sources, i.e., both the current density $\boldsymbol{J}$ and volume charge density ρ are equal to 0, the phasors $\boldsymbol{E}(\boldsymbol{r})$ and $\boldsymbol{H}(\boldsymbol{r})$ satisfy the Maxwell equations in the phasor domain:

$$\nabla \times \boldsymbol{E} = -j\omega\mu\boldsymbol{H} \tag{C.2a}$$
$$\nabla \times \boldsymbol{H} = j\omega\varepsilon\boldsymbol{E} \tag{C.2b}$$
$$\nabla \cdot \varepsilon\boldsymbol{E} = 0 \tag{C.2c}$$
$$\nabla \cdot \mu\boldsymbol{H} = 0 \tag{C.2d}$$

where ω is the angular frequency. $\varepsilon = \varepsilon_0\varepsilon_r$ and $\mu = \mu_u\mu_r$ are the permittivity and permeability of the medium, respectively, and can be written as product between vacuum (ε_0, μ_0) and relative parameters (ε_r, μ_r). Although not explicitly expressed in Eqs. (C.2), in general, both the fields and the material parameters are functions of the position vector $\boldsymbol{r}$, $\boldsymbol{E}(\boldsymbol{r})$, $\boldsymbol{H}(\boldsymbol{r})$, $\varepsilon(\boldsymbol{r})$, $\mu(\boldsymbol{r})$.

In case of a plane wave in a homogeneous medium, the solution of Maxwell equations is

$$\begin{aligned}\boldsymbol{E}(\boldsymbol{r}) &= \boldsymbol{E}_0 e^{-jk_0 n(\hat{\boldsymbol{k}}\cdot\boldsymbol{r})}\\ \boldsymbol{H}(\boldsymbol{r}) &= \boldsymbol{H}_0 e^{-jk_0 n(\hat{\boldsymbol{k}}\cdot\boldsymbol{r})}\end{aligned} \tag{C.3}$$

where $n = \sqrt{\varepsilon_r\mu_r}$ is the refractive index, k_0 is the vacuum wavenumber, and $\hat{\boldsymbol{k}}$ is the unit vector along the propagation direction. For example, in free-space, $n = 1$ and the field becomes simply

$$\begin{aligned}\boldsymbol{E}(\boldsymbol{r}) &= \boldsymbol{E}_0 e^{-jk_0 r}\\ \boldsymbol{H}(\boldsymbol{r}) &= \boldsymbol{H}_0 e^{-jk_0 r}.\end{aligned} \tag{C.4}$$

Note that $\boldsymbol{E}_0$ and $\boldsymbol{H}_0$ are complex vector amplitudes that are constant with $\boldsymbol{r}$ only for plane waves. When observing the plane wave solutions in Equation C.4, one can infer that more general a wave propagating far away (many wavelengths) from the sources can be represented by

$$\begin{aligned} \boldsymbol{E}(\boldsymbol{r}) &= \boldsymbol{E}_0(\boldsymbol{r})e^{-jk_0S(\boldsymbol{r})} \\ \boldsymbol{H}(\boldsymbol{r}) &= \boldsymbol{H}_0(\boldsymbol{r})e^{-jk_0S(\boldsymbol{r})}. \end{aligned} \tag{C.5}$$

In Equation C.5, $S(\boldsymbol{r})$ is a scalar function that we define as "optical path". $\boldsymbol{E}_0(\boldsymbol{r})$ and $\boldsymbol{H}_0(\boldsymbol{r})$ are vector functions. Using Equation C.5 as a trial solution to the Maxwell equations, $\boldsymbol{E}_0(\boldsymbol{r})$, $\boldsymbol{H}_0(\boldsymbol{r})$ and S can be related. Substitute (C.5) in (C.2), which leads to the following algebraic steps:

Eq. (C.2b)	$\nabla \times \boldsymbol{H} = -j\omega\varepsilon\boldsymbol{E}$
Replacing Eq. (C.5) in Eq. (C.2b)	$\nabla \times (\boldsymbol{H}_0 e^{-jk_0S}) = j\omega\varepsilon\boldsymbol{E}_0 e^{-jk_0S}$
Using the identity $\nabla \times (\psi\boldsymbol{A}) = \nabla\psi \times \boldsymbol{A} + \psi\nabla \times \boldsymbol{A}$ (for scalar field ψ and vector field $\boldsymbol{A}$)	$\nabla e^{-jk_0S} \times \boldsymbol{H}_0 + e^{-jk_0S}\nabla \times \boldsymbol{H}_0 = j\omega\varepsilon\boldsymbol{E}_0 e^{-jk_0S}$
$\nabla e^{-jk_0S} = -jk_0 e^{-jk_0S}\nabla S$	$-jk_0 e^{-jk_0S}\nabla S \times \boldsymbol{H}_0 + e^{-jk_0S}\nabla \times \boldsymbol{H}_0 = j\omega\varepsilon\boldsymbol{E}_0 e^{-jk_0S}$
Dividing by e^{-jk_0S}	$-jk_0\nabla S \times \boldsymbol{H}_0 + \nabla \times \boldsymbol{H}_0 = j\omega\varepsilon\boldsymbol{E}_0$
Dividing by $-jk_0$	$\nabla S \times \boldsymbol{H}_0 + \varepsilon c_0\boldsymbol{E}_0 = \dfrac{1}{jk_0}\nabla \times \boldsymbol{H}_0$ where $c_0 = \omega/k_0$ is the speed of light
Eq. (C.2a)	$\nabla \times \boldsymbol{E} = -j\omega\mu\boldsymbol{H}$
Equivalent steps as for Eq. (C.2b)	$\nabla S \times \boldsymbol{E}_0 - \mu c_0\boldsymbol{H}_0 = \dfrac{1}{jk_0}\nabla \times \boldsymbol{E}_0$
Eq. (C.2c)	$\nabla \cdot \varepsilon\boldsymbol{E} = 0$
Replacing Eq. (C.5) in Eq. (C.2c)	$\nabla \cdot \varepsilon\boldsymbol{E}_0 e^{-jk_0S} = 0$
Using the identity $\nabla \cdot (\psi\phi\boldsymbol{A}) = (\phi\nabla\psi + \psi\nabla\phi) \cdot \boldsymbol{A} + \psi\phi\nabla \cdot \boldsymbol{A}$ (for scalar fields ψ, ϕ and vector field $\boldsymbol{A}$)	$\left(\varepsilon\nabla e^{-jk_0S} + e^{-jk_0S}\nabla\varepsilon\right) \cdot \boldsymbol{E}_0 + \varepsilon e^{-jk_0S}\nabla \cdot \boldsymbol{E}_0 = 0$
$\nabla e^{-jk_0S} = -jk_0 e^{-jk_0S}\nabla S$	$-\varepsilon jk_0 e^{-jk_0S}\nabla S \cdot \boldsymbol{E}_0 + e^{-jk_0S}\nabla\varepsilon \cdot \boldsymbol{E}_0 + \varepsilon e^{-jk_0S}\nabla \cdot \boldsymbol{E}_0 = 0$
Dividing by e^{-jk_0S}	$-\varepsilon jk_0\nabla S \cdot \boldsymbol{E}_0 + \nabla\varepsilon \cdot \boldsymbol{E}_0 + \varepsilon\nabla \cdot \boldsymbol{E}_0 = 0$
Dividing by $-jk_0\varepsilon$	$\nabla S \cdot \boldsymbol{E}_0 = \dfrac{-\boldsymbol{E}_0 \cdot \nabla\varepsilon - \varepsilon\nabla \cdot \boldsymbol{E}_0}{-jk_0\varepsilon}$
Noting that $\nabla \ln\varepsilon = \frac{1}{\varepsilon}\nabla\varepsilon$	$\nabla S \cdot \boldsymbol{E}_0 = \dfrac{1}{jk_0}\left(\boldsymbol{E}_0 \cdot \nabla \ln\varepsilon + \nabla \cdot \boldsymbol{E}_0\right)$
Eq. (C.2d)	$\nabla \cdot \mu\boldsymbol{H} = 0$
Equivalent steps as for Eq. (C.2c)	$\nabla S \cdot \boldsymbol{H}_0 = \dfrac{1}{jk_0}\left(\boldsymbol{H}_0 \cdot \nabla \ln\mu + \nabla \cdot \boldsymbol{H}_0\right)$

Summarizing the results:

$$\nabla S \times \boldsymbol{H}_0 + \varepsilon c_0\boldsymbol{E}_0 = \frac{1}{jk_0}\nabla \times \boldsymbol{H}_0 \tag{C.6a}$$

$$\nabla S \times \boldsymbol{E}_0 - \mu c_0\boldsymbol{H}_0 = \frac{1}{jk_0}\nabla \times \boldsymbol{E}_0 \tag{C.6b}$$

$$\nabla S \cdot \boldsymbol{E}_0 = \frac{1}{jk_0}(\boldsymbol{E}_0 \cdot \nabla \ln\varepsilon + \nabla \cdot \boldsymbol{E}_0) \tag{C.6c}$$

$$\nabla S \cdot \boldsymbol{H}_0 = \frac{1}{jk_0}(\boldsymbol{H}_0 \cdot \nabla \ln\mu + \nabla \cdot \boldsymbol{H}_0) \tag{C.6d}$$

In the geometrical optics approximation, large k_0 is considered. For $k_0 \to \infty$, the equations simplify to

$$\nabla S \times \boldsymbol{H}_0 = -\varepsilon c_0 \boldsymbol{E}_0 \tag{C.7a}$$
$$\nabla S \times \boldsymbol{E}_0 = \mu c_0 \boldsymbol{H}_0 \tag{C.7b}$$
$$\nabla S \cdot \boldsymbol{E}_0 = 0 \tag{C.7c}$$
$$\nabla S \cdot \boldsymbol{H}_0 = 0\,. \tag{C.7d}$$

From (C.7a), one can write

$$\boldsymbol{E}_0 = -\frac{1}{\varepsilon c_0} \nabla S \times \boldsymbol{H}_0. \tag{C.8}$$

Placing the result in (C.7b) and applying the vector triple product identity yields

$$\frac{1}{\varepsilon c_0}[(\nabla S \cdot \boldsymbol{H}_0)\nabla S - (\nabla S)^2 \boldsymbol{H}_0] = -\mu c_0 \boldsymbol{H}_0. \tag{C.9}$$

Using (C.7d), this is reduced to

$$\frac{1}{\varepsilon c_0}\left[-(\nabla S)^2 \boldsymbol{H}_0\right] = -\mu c_0 \boldsymbol{H}_0 \tag{C.10}$$

Which results in

$$(\nabla S)^2 = \varepsilon \mu c_0^2\,. \tag{C.11}$$

Note that $\varepsilon\mu = \varepsilon_0 \varepsilon_r \mu_0 \mu_r = n^2 \left(\sqrt{\varepsilon_0 \mu_0}\right)^2 = \frac{n^2}{c_0^2}$:

$$(\nabla S)^2 = \frac{n^2}{c_0^2} c_0^2 \tag{C.12}$$

which leads to

$$(\nabla S)^2 = n^2. \tag{C.13}$$

(C.13) is called the *Eikonal Equation*, S is called the Eikonal, and $S(\boldsymbol{r}) = \text{const.}$ represents geometrical wavefronts. Written explicitly in a cartesian coordinate system as

$$\left(\frac{\partial S}{\partial x}\right)^2 + \left(\frac{\partial S}{\partial y}\right)^2 + \left(\frac{\partial S}{\partial z}\right)^2 = n^2(x, y, z)\,. \tag{C.14}$$

C.2 Light Rays

The Poynting vector for the wave expressed in (C.5) can be written as

$$\boldsymbol{S} = \frac{1}{2}\boldsymbol{E} \times \boldsymbol{H}^* = \frac{1}{2}\boldsymbol{E}_0 e^{-jk_0 S} \times \boldsymbol{H}_0^* e^{jk_0 S} = \frac{1}{2}\boldsymbol{E}_0 \times \boldsymbol{H}_0^*. \tag{C.15}$$

By using Eq. (C.7b) and assuming a losseless medium (μ is a real function)

$$\boldsymbol{S} = \frac{1}{2}\left(\boldsymbol{E}_0 \times \frac{1}{\mu c_0}\left(\nabla S \times \boldsymbol{E}_0^*\right)\right) = \frac{1}{2\mu c_0}\left(\boldsymbol{E}_0 \times \nabla S \times \boldsymbol{E}_0^*\right) \tag{C.16}$$

which, using the vector triple product identity can be reduced to:

$$\boldsymbol{S} = \frac{1}{2\mu c_0}\left(|\boldsymbol{E}_0|^2 \nabla S - (\boldsymbol{E}_0 \cdot \nabla S)\,\boldsymbol{E}_0^*\right)\,. \tag{C.17}$$

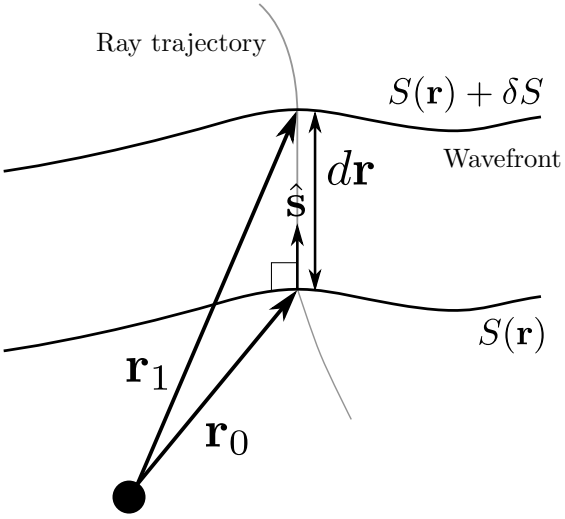

Figure C.1: A ray trajectory passing through two wavefronts. Note that $d\boldsymbol{r}$ is pointing in the same direction as $\boldsymbol{s}$ and when $d\boldsymbol{r}$ is scaled with ds, the vectors are equal.

From Eq. (C.7c)

$$\boldsymbol{S} = \frac{|\boldsymbol{E}_0|^2}{2\mu c_0}\nabla S = \frac{|\boldsymbol{E}_0|^2}{2\zeta}\nabla S \tag{C.18}$$

where $\zeta = \sqrt{\mu/\varepsilon}$ is the medium impedance. From the Eikonal Equation Eq. (C.13), one can also write

$$|\nabla S| = n. \tag{C.19}$$

Thus, the vector $\boldsymbol{s}$, defined as

$$\boldsymbol{s} = \frac{\nabla S}{|\nabla S|} = \frac{\nabla S}{n} \tag{C.20}$$

is a unit vector in the same directions as the Poynting vector.

The geometrical light rays can be defined as orthogonal trajectories to the geometrical wavefronts $S = \text{const}$. If $\boldsymbol{r}(s)$ is the position vector of a point on a ray, as a function of the length of arc s of the ray, then we have

$$\frac{d\boldsymbol{r}(s)}{ds} = \boldsymbol{s}. \tag{C.21}$$

In Fig. C.1 this situation is shown. If the difference between the points on a ray is made sufficiently small, the ray path coincides with $\boldsymbol{r}_0 - \boldsymbol{r}_1$.

Now, using Eq. (C.20) and Eq. (C.21) one can write

$$n\frac{d\boldsymbol{r}(s)}{ds} = \nabla S\,. \tag{C.22}$$

The optical length of a path between two points P_1 and P_2 can be found as

$$\int_{P_1}^{P_2} n ds = S\left(P_2\right) - S\left(P_1\right)\,. \tag{C.23}$$

From Eq. (C.22), one can find the differential equations of the light rays by applying the following algebraic steps:

Eq. (C.22)	$n\frac{d\boldsymbol{r}(s)}{ds} = \nabla S$
Differentiating Eq. (C.22) with respect to s	$\frac{d}{ds}\left(n\frac{d\boldsymbol{r}(s)}{ds}\right) = \frac{d}{ds}(\nabla s)$
The derivative $\frac{d}{ds}$ is equivalent to the operation $\frac{d\boldsymbol{r}}{ds}\cdot\nabla$ $\frac{d\boldsymbol{r}}{ds} = \frac{d(x\hat{x}+y\hat{y}+z\hat{z})}{ds} = \left(\frac{dx}{ds},\frac{dy}{ds},\frac{dz}{ds}\right)$ $\nabla = \left(\frac{d}{dx},\frac{d}{dy},\frac{d}{dz}\right)$ $\frac{d\boldsymbol{r}}{ds}\cdot\nabla = \left(\frac{dx}{ds},\frac{dy}{ds},\frac{dz}{ds}\right)\cdot\left(\frac{d}{dx},\frac{d}{dy},\frac{d}{dz}\right) = \frac{d}{ds}$	$\frac{d}{ds} = \frac{d\boldsymbol{r}}{ds}\cdot\nabla$
Substituting $\frac{d}{ds} = \frac{d\boldsymbol{r}}{ds}\cdot\nabla$ in $\frac{d}{ds}\left(n\frac{d\boldsymbol{r}(s)}{ds}\right) = \frac{d}{ds}(\nabla s)$ Using Eq. (C.20) Using the property $\nabla\left[(\nabla S)^2\right] = 2\nabla S\cdot\nabla(\nabla S)$ $\nabla n^2 = 2n\nabla n$	$\frac{d}{ds}\left(n\frac{d\boldsymbol{r}(s)}{ds}\right) = \frac{d\boldsymbol{r}}{ds}\cdot\nabla(\nabla S) = \frac{\nabla S}{n}\cdot\nabla(\nabla S) = \frac{1}{2n}\nabla\left[(\nabla S)^2\right]$ $\frac{d}{ds}\left(n\frac{d\boldsymbol{r}(s)}{ds}\right) = \frac{1}{2n}\nabla n^2$ $\frac{d}{ds}\left(n\frac{d\boldsymbol{r}(s)}{ds}\right) = \nabla n$

These steps yield the differential equation of the light rays:

$$\frac{d}{ds}\left(n\frac{d\boldsymbol{r}(s)}{ds}\right) = \nabla n\,. \tag{C.24}$$

C.3 Steps for Ordinary Differential Equations (ODE) System

One can derive an ordinary differential equations (ODE) system to solve these equations. Writing Eq. (C.22) in terms of its different components explicitly

$$n\frac{dx}{ds}\hat{\boldsymbol{x}} + n\frac{dy}{ds}\hat{\boldsymbol{y}} + n\frac{dz}{ds}\hat{\boldsymbol{z}} = \frac{\partial S}{\partial x}\hat{\boldsymbol{x}} + \frac{\partial S}{\partial y}\hat{\boldsymbol{y}} + \frac{\partial S}{\partial z}\hat{\boldsymbol{z}} \tag{C.25}$$

and defining $p_x = \frac{\partial S}{\partial x}$, $p_y = \frac{\partial S}{\partial y}$ and $p_z = \frac{\partial S}{\partial z}$, yields 3 scalar equations.

$$n\frac{dx}{ds} = p_x \tag{C.26a}$$

$$n\frac{dy}{ds} = p_y \tag{C.26b}$$

$$n\frac{dz}{ds} = p_z \tag{C.26c}$$

Similar for Eq. (C.24), one can write explicitly

$$\frac{d}{ds}\left(n\frac{dx}{ds}\right)\hat{\boldsymbol{x}} + \frac{d}{ds}\left(n\frac{dy}{ds}\right)\hat{\boldsymbol{y}} + \frac{d}{ds}\left(n\frac{dz}{ds}\right)\hat{\boldsymbol{z}} = \left(\frac{\partial n}{\partial x}\hat{\boldsymbol{x}} + \frac{\partial n}{\partial y}\hat{\boldsymbol{y}} + \frac{\partial n}{\partial z}\hat{\boldsymbol{z}}\right). \tag{C.27}$$

Using Eq. (C.26), 3 scalar equations can be written:

$$\frac{dp_x}{ds} = \frac{\partial n}{\partial x} \tag{C.28a}$$
$$\frac{dp_y}{ds} = \frac{\partial n}{\partial y} \tag{C.28b}$$
$$\frac{dp_z}{ds} = \frac{\partial n}{\partial z} \tag{C.28c}$$

The combination of Eq. (C.26) and Eq. (C.28) yields the full ODE system. To solve it, a numerical solver can be used to solve the initial value problem, where the initial values are given by

$$x = x_0 \tag{C.29a}$$
$$y = y_0 \tag{C.29b}$$
$$z = z_0 \tag{C.29c}$$
$$p_x = n(x_0, y_0, z_0)\sin\theta\cos\phi \tag{C.29d}$$
$$p_y = n(x_0, y_0, z_0)\sin\theta\sin\phi \tag{C.29e}$$
$$p_z = n(x_0, y_0, z_0)\cos\phi \tag{C.29f}$$

Numerical solvers, such as the `ode45` solver from MATLAB can be used to solve such problems.